

**Verification of land-atmosphere coupling in forecast models, reanalyses and land surface  
models using flux site observations**

Paul A. Dirmeyer<sup>1\*</sup>, Liang Chen<sup>1</sup>, Jiexia Wu<sup>1</sup>, Chul-Su Shin<sup>1</sup>, Bohua Huang<sup>1</sup>, Benjamin A. Cash<sup>1</sup>, Michael G. Bosilovich<sup>2</sup>, Sarith Mahanama<sup>2</sup>, Randal D. Koster<sup>2</sup>, Joseph A. Santanello<sup>2</sup>, Michael B. Ek<sup>3</sup>, Gianpaolo Balsamo<sup>4</sup>, Emanuel Dutra<sup>5</sup>, and D. M. Lawrence<sup>6</sup>

<sup>1</sup>Center for Ocean-Land-Atmosphere Studies, George Mason University

<sup>2</sup>NASA / Goddard Space Flight Center

<sup>3</sup>NOAA / National Centers for Environmental Prediction / Environmental Modeling Center

<sup>4</sup>European Centre for Medium-range Weather Forecasts

<sup>5</sup>Instituto Dom Luiz, Faculdade de Ciências, Universidade de Lisboa<sup>5</sup>National Center for Atmospheric Research

\*Corresponding Author:

Paul A. Dirmeyer  
Center for Ocean-Land-Atmosphere Studies  
George Mason University  
4400 University Drive, Mail Stop: 6C5  
Fairfax, Virginia 22030 USA  
*pdirmeye@gmu.edu*

Submitted to: *Journal of Hydrometeorology*

1    **Abstract:**

2    We confront four model systems in three configurations (LSM, LSM+GCM, and  
3    reanalysis) with global flux tower observations to validate states, surface fluxes, and  
4    coupling indices between land and atmosphere. Models clearly under-represent the  
5    feedback of surface fluxes on boundary layer properties (the atmospheric leg of land-  
6    atmosphere coupling), and may over-represent the connection between soil moisture and  
7    surface fluxes (the terrestrial leg). Models generally under-represent spatial and temporal  
8    variability relative to observations, which is at least partially an artifact of the differences  
9    in spatial scale between model grid boxes and flux tower footprints. All models bias high in  
10   near-surface humidity and downward shortwave radiation, struggle to represent  
11   precipitation accurately, and show serious problems in reproducing surface albedos. These  
12   errors create challenges for models to partition surface energy properly and errors are  
13   traceable through the surface energy and water cycles. The spatial distribution of the  
14   amplitude and phase of annual cycles (first harmonic) are generally well reproduced, but  
15   the biases in means tend to reflect in these amplitudes. Interannual variability is also a  
16   challenge for models to reproduce. Our analysis illuminates targets for coupled land-  
17   atmosphere model development, as well as the value of long-term globally-distributed  
18   observational monitoring.

19

20 **1. Introduction**

21 Many LSMs were developed and pressed into service during the 1980s and 1990s to  
22 provide lower boundary conditions for the atmospheric GCMs used in climate and weather  
23 simulation and prediction (Santanello et al. 2017). This occurred at a time when  
24 observations of key land surface variables, and the coupled processes that link the water  
25 and energy cycles between the land and atmosphere, were extremely limited. As a result,  
26 performance of coupled LSM-GCM systems has been sub-optimal (Dirmeyer et al. 2017).

27 The necessary observational data sets for validation are only recently becoming  
28 available; datasets that combine co-located measurements of land surface states, surface  
29 fluxes, near-surface meteorology, and properties of the atmospheric column. Early field  
30 campaigns (e.g., Sellers et al. 1992, 1995; Famiglietti et al. 1999; Jackson and Hsu 2001;  
31 Andreae 2002) provided observations that helped advance theory and model  
32 parameterization development, but their short periods of operation meant collected data  
33 provided limited sampling of the phase-space of land-atmosphere interactions, rarely  
34 quantifying interannual variability. In the mid-1990s, networks of observing stations began  
35 to be established and maintained, providing long-term data sets. A growing number of soil  
36 moisture monitoring networks have been established. Their data have been collated,  
37 homogenized and standardized by two separate efforts (Dorigo et al. 2011, 2013, 2017;  
38 Quiring et al. 2016). Those data sets were used by Dirmeyer et al. (2016) in a first-of-its-  
39 kind multi-model multi-configuration assessment of soil moisture simulation fidelity.

40 Simultaneously, efforts began in the ecological community to collect surface flux data  
41 over a variety of biomes (FLUXNET; Baldocchi et al 2001). Over time, in consultation with  
42 interested scientific communities, FLUXNET expanded their instrumentation suite to  
43 measure soil moisture, ground heat flux, and four-component radiation, allowing detailed

44 closure of the surface energy balance. Rigid standards for data formatting and  
45 dissemination within and across regional networks was lacking, so a global standardized  
46 and quality-controlled subset of data from many FLUXNET sites was produced (“La Thuile  
47 FLUXNET dataset”, cf. <http://www.fluxdata.org>) covering multiple links in the coupled  
48 land-atmosphere process chain (Santanello et al. 2011). The La Thuile data set enabled a  
49 greater degree of model validation (e.g., Williams et al. 2009; Bonan et al. 2012; Boussetta  
50 et al. 2013; Melaas et al. 2013; Balzarolo et al. 2014; Purdy et al. 2016).

51 In this study, we employ the updated FLUXNET2015 synthesis data set, (Pastorello et al.  
52 2017) expanding the multi-model multi-configuration study of soil moisture simulations in  
53 Dirmeyer et al. (2016) to a global assessment of surface energy and water balance  
54 simulations, and basic metrics of land-atmosphere coupling. Section 2 describes the  
55 observational data and models examined. The next three sections present validations of  
56 model annual means, annual cycles, and coupling metrics. We then discuss some of the  
57 pathological model behaviors that emerge from the analysis and present conclusions.  
58 Throughout the paper we present synthesis figures. Detailed scatter plots showing results  
59 across all FLUXNET2015 sites for each model are consigned to the Supplement.

60

## 61 **2. Data and Models**

62 The range of dates of data varies considerably among model simulations, and also  
63 between individual observational sites. We analyze spatial variability and compare only  
64 climatologies (annual means or mean annual cycles) in order to minimize the effect of such  
65 asynchronicities, and present a quantification of interannual variability. It is not the intent  
66 of this study to validate model simulations of specific events, but rather their overall  
67 coupled land-atmosphere behavior. Note also that many coupling metrics, including those

68 used here, can be calculated for LSMs from a combination of forcing and model output,  
69 even though the LSMs are not coupled to GCMs.

70 *2.1 Observed data*

71 In situ measurements of near surface meteorological variables, surface fluxes and soil  
72 moisture used for model validation come from the November 2016 version of the  
73 FLUXNET2015 station data set. Daily, monthly and yearly data have been used; processing  
74 of the meteorological, radiation, heat flux and surface hydrologic data including gap-filling  
75 are described by Reichstein et al. (2005) and Vuichard and Papale (2015). Only the Tier 1  
76 (open access) data are used in this study (see Table S1 for a complete list of sites) – Figure  
77 1 shows the spatial distribution of sites and some of the key characteristics regarding data  
78 availability. 166 sites provide 1242 site-years of data, but coverage is concentrated in the  
79 mid-latitudes and particular underrepresentation in the tropics.

80 The variables processed for this analysis include surface pressure, near surface air  
81 temperature and vapor pressure deficit, precipitation, four-component and net radiation,  
82 surface sensible and latent heat fluxes (gap-filled following the method of Reichstein et al.  
83 2005 and energy balance closure-corrected) and soil water content measured at the first  
84 (shallowest) sensor. There is no consolidated information on the depth of the shallowest  
85 sensor across all sites, but typically it is at 5cm or 10cm below the surface. Vapor pressure  
86 deficit is converted to specific humidity using the Clausius-Clapeyron relationship. We have  
87 used the provided FLUXNET2015 data at the corresponding time intervals for each  
88 calculation: yearly data for annual means, monthly data for annual cycles, and daily data for  
89 calculating coupling indices.

90 In addition, we examine a number of gridded global precipitation products for  
91 comparison to FLUXNET2015 sites. These are listed in Table S2.

92 *2.2 Model systems*

93 Four global modeling systems are evaluated; two from operational forecast centers and  
94 two that are primarily used for research. The operational systems are from the U.S.  
95 National Oceanic and Atmospheric Administration (NOAA) National Centers for  
96 Environmental Prediction (NCEP) and the European Centre for Medium-range Weather  
97 Forecasts (ECMWF). The research systems are from the U.S. National Aeronautics and  
98 Space Administration (NASA) Global Modeling and Assimilation Office (GMAO) and the U.S.  
99 National Center for Atmospheric Research (NCAR).

100 Table 1 summarizes the model components and configurations. Generally, each  
101 modeling system is interrogated in three different configurations: 1) LSM only (offline),  
102 driven by gridded observationally-based meteorological analyses including downward  
103 radiation; 2) LSM coupled to GCM in a *free-running* mode where the coupled system  
104 evolves unconstrained after initialization; 3) Reanalysis, where the coupled LSM and GCM  
105 are constrained by data assimilation at diurnal or sub-diurnal increments to represent the  
106 actual historical evolution of state variables. The NCAR model system does not have an  
107 associated reanalysis, so to keep the four-by-three matrix filled, two different reanalyses  
108 from GMAO are included. Note that when the coordinates for a FLUXNET2015 site lie  
109 within a model's ocean grid cell, it is excluded from comparisons for that model. Thus, the  
110 number of stations compared vary from model to model depending on resolution and the  
111 land-sea mask.

112 2.2.1 NCEP

113 Data for the offline configuration comes from an author-produced simulation using Noah  
114 LSM version 2.7.1 (Ek et al., 2003, Mitchell, 2005) driven by 3-hourly gridded  
115 meteorological data from the Terrestrial Hydrology Research Group at Princeton

116 University (Sheffield et al., 2006). The free-running coupled land-atmosphere simulation  
117 consists of a subset of 48 years from a 420 year long current climate simulation of CFSv2  
118 initialized in 1980 (Shukla et al. 2017). The coupled simulation is unique among the model  
119 systems in that it also includes a coupled ocean component. However, this should have very  
120 little effect on the local coupled land-atmosphere behavior of the model. Years 2101-2148  
121 of the simulation are used, but the calendar dates have no real meaning in a fully coupled  
122 climate model so far from the initial state, wherein attributes such as atmospheric  
123 composition, solar intensity, orbital parameters, etc., are held constant at late 20th century  
124 values. The latest NCEP reanalysis is also examined (CFSR; Saha et al. 2010), which  
125 combines a global land data assimilation system derived from the NASA Land Information  
126 System (LIS; Peters-Lidard et al., 2007), driven by a blended global precipitation analysis  
127 (Xie and Arkin 1997; Xie et al. 2007), used to update the coupled analysis cycle once per  
128 day over the period 1979-2009.

129 2.2.2 GMAO

130 Two reanalyses are included for GMAO; version 1 and version 2 of the Modern-Era  
131 Retrospective Analysis for Research and Applications (MERRA; Rienecker et al. 2011,  
132 Reichle et al. 2017a). MERRA data cover the period 1980-2015. MERRA-2 is the current  
133 state-of-the-art reanalysis covering 1980-2015 (Molod et al. 2015, Gelaro et al. 2017), and  
134 is the source of most of the meteorological forcing data for the offline simulation of the  
135 Catchment LSM v25 C05 (GMAO 2015a,b). As part of the MERRA-2 reanalysis, the GCM-  
136 generated precipitation is corrected with observations-based precipitation before it  
137 reaches the land surface (Reichle et al. 2017b); the reanalysis meteorological fields thus  
138 feel the observed precipitation rates indirectly through the surface fluxes. Additionally, a  
139 global 36-year offline Catchment simulation on the MERRA grid and a 16-year coupled

140 GEOS5-Catchment simulation at half-degree resolution with prescribed observed SSTs  
141 were generated for this comparison.

142 2.2.3 NCAR

143 There is no operational reanalysis produced with the NCAR Community Earth System  
144 Model (CESM). However, CESM is widely used for research in the academic community,  
145 and we have generated offline and coupled simulations for this comparison. The offline  
146 simulation uses version 4.5 of the Community Land Model (CLM; Lawrence et al. 2011)  
147 driven with forcing spanning 1991-2010 from version 4 of the blended and gap-filled  
148 CRUNCEP (Viovy 2013)  $0.5^\circ$  data set (available at:  
149 <https://www.earthsystemgrid.org/dataset/ucar.cgd.ccsm4.CRUNCEP.v4.html>) aggregated  
150 to the nominal  $1^\circ$  GCM resolution. A simulation with CLM4.5 coupled to CAM4 in CESM1.2.2  
151 has been produced spanning 1991-2014 with specified climatological SSTs.

152 2.2.4 ECMWF

153 The offline simulation from ECMWF is with Cycle 43R1 of the Hydrology Tiled ECMWF  
154 Scheme of Surface Exchanges over Land (HTESSEL) run at  $\sim 16\text{km}$  resolution based on a  
155 cubic octahedral global grid (TCO639) for the period 1979-2015. This offline simulation  
156 follows ERA-Interim/land configurations closely (see Balsamo et al. 2015), forced by ERA-  
157 Interim meteorology and fluxes with **an altitude correction applied to temperature,**  
158 **humidity and surface pressure.** This offline simulation is used to initialized the land state of  
159 the operational ECMWF hindcasts. The coupled simulation comes from the Athena Project  
160 (Kinter et al. 2013) for 1961-2007 where an older version of HTESSEL is coupled to IFS  
161 Cycle 32R3 at a similarly high native horizontal resolution and specified observed SSTs, but  
162 the data has been post-processed to a  $1.125^\circ$  uniform grid. ERA-Interim (Dee et al. 2011),

163 spanning 1979-2015, provides the reanalysis configuration of data for the comparison,  
164 which used TESSEL prior to hydrology upgrades.

165

166 **3. Annual Means**

167 The comparison of models to FLUXNET2015 observations of annual means amounts to  
168 an assessment of model ability to reproduce global spatial patterns (within the limitations  
169 of the uneven distribution of station locations) of the variables' time averages. For the  
170 offline LSM simulations, meteorological forcing data are specified from gridded data sets,  
171 so their correlation to FLUXNET2015 observations is not a pure reflection of model  
172 performance as the forcing data constrain LSM behavior. Similarly, for the reanalysis  
173 products, performance reflects a combination of model characteristics, data assimilation  
174 techniques and the distribution and quality of the data assimilated. Assimilation of  
175 observational data constrains the coupled land-atmosphere model behavior to some  
176 degree. While the free-running model simulations provide an unabridged assessment of  
177 model performance, results from the other modes of simulation are nevertheless  
178 enlightening.

179 As an indicator of observational uncertainty and the impact of comparing model grid  
180 box values to field sites, we first note how a number of gridded observational precipitation  
181 products and the reanalyses validate against precipitation measurements at FLUXNET2015  
182 locations. Figure 2 shows mean (dots) and span (whiskers) of annual precipitation totals,  
183 where the abscissa always corresponds to measurements from the FLUXNET2015 sites.  
184 For most sites, the observational products (top two rows of Fig. 2) cover the entire time  
185 span of FLUXNET2015 observations (see Table S2 for details). All reanalyses (bottom row  
186 of Fig. 2) except CFSR span the FLUXNET2015 period. Several statistics of spatial

187 agreement are shown: Pearson's product moment correlation coefficient ( $r_p$ ), Spearman's  
188 rank correlation coefficient ( $r_s$ ), root mean square error (RMSE), slope of the best-fit linear  
189 regression of Y on X (Slope) and the fraction of total stations (labeled "Span Diag" in Fig. 2)  
190 where the span of the individual annual totals from the gridded products (vertical  
191 whiskers) overlap the span from FLUXNET2015 sites (horizontal whiskers). The last  
192 statistic tests the possibility that the FLUXNET2015 observations and gridded estimates do  
193 not come from distinct populations, i.e. their ranges overlap.

194 Estimates from gridded observational data sets, which range in spatial resolution from  
195 0.25° (MSWEP, TRMM) to 2.5° (GPCP), provide a plausible upper bound to the accuracy we  
196 could expect from gridded Earth system models. For the 166 (or fewer) FLUXNET2015  
197 sites compared, which admittedly represent a rather uneven sampling of global terrestrial  
198 precipitation, three observational products score at the top: MSWEP, CPC-Uni and U.Del.  
199 Each has a Pearson's correlation of nearly 0.8, a rank correlation between 0.8-0.9, and the  
200 highest number of stations whose ranges span the diagonal X=Y line. The lower limit for  
201 RMSE across these sites is about 240mm. Note that all gridded products underestimate the  
202 slope, indicating the inability of large area averages to resolve local variations in average  
203 precipitation.

204 MERRA-2 performs on par with the best gridded observed products, namely because it  
205 reports a bias corrected precipitation that is used as part of the assimilation process  
206 instead of model-generated precipitation as an input to the LSM (Reichle and Liu 2014).  
207 Thus, it is effectively another gridded observational data set for precipitation. Figure S1  
208 compares the precipitation predicted by the model physical parameterizations in MERRA-2  
209 alongside the corrected version in the same fashion as Fig 2. The correction greatly reduces  
210 bias, cuts RMSE by one third, slightly improves spatial correlations, and increases the

211 number of stations spanning the diagonal by 28%. CFSR significantly underperforms other  
212 reanalyses at FLUXNET2015 locations.

213 Precipitation is among the most difficult quantities for models to simulate. We expect  
214 among near surface meteorological variables the lowest correlations and largest coefficient  
215 of variation for precipitation. It also has many observationally-based data sets to choose  
216 from, providing a robust estimate of skill to be expected from comparing point  
217 measurements to gridded data sets. Figure 2 provides generous thresholds, particularly for  
218 correlations, to keep in mind when assessing model simulations of the terms of the surface  
219 water and energy balance. As shown below, correlations of 0.7-0.8 are a challenge for  
220 models to attain for precipitation, as well as some other water and energy budget terms.

221 Among near surface meteorology (e.g., temperature and specific humidity) and  
222 downward surface fluxes (including shortwave and longwave radiation), precipitation has  
223 the greatest small-scale variability on monthly to annual time scales, and is thus the most  
224 difficult land surface “forcing” to replicate at the FLUXNET2015 sites. Figures S2-S6 show  
225 the scatters and statistics for the models listed in Table 1 for these five variables. Here, the  
226 restriction that the years of the models match those at each FLUXNET2015 site is lifted, and  
227 the climatologies of the complete data sets are compared. Not surprisingly, the global  
228 distribution of annual mean temperature is very well reproduced by the models (Fig. S2),  
229 with 88-96% of the observed variance explained. Observed specific humidity is only  
230 slightly less well correlated among the models (Fig. S3), but there is a consistent positive  
231 bias relative to FLUXNET2015 measurements. Patterns of annual mean downward  
232 radiation (Figs. S4 and S5) are well simulated, with a tendency for a slight negative bias in  
233 longwave radiation (Fig. S5), and a stronger positive bias in shortwave radiation across  
234 models (Fig. S4), consistent with other assessments of model shortwave errors that depend

235 on GCM radiative transfer parameterizations (cf. Slater 2016). Precipitation shows the least  
236 agreement; note the bottom row of Fig. S6 is not identical to that of Fig. 2 because the years  
237 compared differ. Nevertheless, the results are similar. We can consider MERRA-2 as  
238 representing the upper limit of comparison for annual precipitation when the periods do  
239 not match between models and observations. Offline Catchment actually performs slightly  
240 better than MERRA-2, and CFSv2 is generally the poorest performing model system in the  
241 set. Free-running climate models understandably perform worse than either reanalyses or  
242 offline LSM simulations, as they are least constrained by observational data. In the case of  
243 CFSv2, there are essentially no constraints within the Earth system as an ocean model is  
244 coupled; other free-running simulations have specified SSTs.

245 Precipitation is a major source of error at the land surface, but so are elements of the  
246 radiation budget. We employ Taylor diagrams to synthesize the statistics of correlation  
247 across FLUXNET2015 sites; RMSE and standard deviation are normalized by observed  
248 values. Figure 3 shows the global distribution of annual mean downward radiation terms is  
249 well simulated across all model configurations, with downward shortwave radiation  
250 performing slightly better than downward longwave radiation. Recall for the LSM-only  
251 models, downward radiation is an input forcing, and the quality of those data sets can vary  
252 significantly (Slater 2016). However, the distribution of upward shortwave radiation is  
253 rather poorly simulated, with the NCEP models showing the worst correlations, and the  
254 NCAR models the best (yet explaining less than half of the variance). There is also a strong  
255 tendency to under-represent the spatial variability (normalized standard deviations less  
256 than 1) of downward shortwave radiation. This degrades simulation of net radiation, which  
257 has consistently lower correlations than downward radiation terms, yet uniformly better  
258 than upward shortwave radiation. The overlap of the spans of annual mean values from

259 models and observations (size of the dots) generally decrease from shortwave down to  
260 longwave down to shortwave up.

261 Figure 3 implies discrepancies in the representation of surface albedo across models at  
262 FLUXNET2015 sites. We show a Taylor diagram for calculated albedo in Fig. 4. As there are  
263 many sites at relatively high northern latitudes that experience snow cover for some part of  
264 the year, snow albedo could specifically be a problem. However, a plot of only the JJA  
265 albedo verification shows boreal summer generally has even lower fidelity, and  
266 systematically low spatial variability, compared to the annual mean. The overlap between  
267 the spans of annual mean albedos range among the models from 16% to 38% of  
268 FLUXNET2015 sites, but for JJA they span only 13-24%.

269 The low variability could be explained by the fact that most LSMs, whether stand-alone  
270 or coupled, have a simple parameterization of albedo based on properties of a small  
271 number of vegetation and soil types, often specified as a climatological seasonal cycle. CLM  
272 actually calculates surface albedo based on a number of properties including vegetation  
273 density and zenith angle of the sun, which may lead to the somewhat better performance of  
274 the NCAR models. As described later, the offline NCEP LSM (identified as NL) specifies a  
275 multi-year satellite-derived monthly green vegetation fraction as a boundary condition that  
276 appears in Fig. 4 to enhance variability, while its positive biases have been noted by Xia et  
277 al. (2012). Furthermore, discrepancies between grid box average albedo and local  
278 conditions at field sites, including the effect of vegetation differences and soil moisture on  
279 albedo (Zaitchik et al. 2013), could add spatial “noise” to the FLUXNET2015 values relative  
280 to what models are representing. Nevertheless, such discrepancies lead to a degradation in  
281 the representation of surface available energy that is partitioned between sensible, latent  
282 and ground heat fluxes. Even an otherwise “perfect” LSM could not produce the right values

283 of these fluxes if net radiation is incorrect. Coupled with errors in precipitation, which  
284 affect available soil moisture and thus Bowen ratios, LSMs are at a compounded  
285 disadvantage in simulating the surface water and energy budget terms.

286 In Fig. 5 we correlate across the stations the mean errors in key water and energy cycle  
287 quantities and present a schematic representation of the relative coupling or  
288 connectedness exhibited between terms. This also suggests how errors in the simulation or  
289 specification of one term can propagate to others through the land-atmosphere coupling  
290 process chain (cf. Santanello et al. 2011).  $r_s$  is generally larger than  $r_p$  because it does not  
291 overemphasize outliers, thus is used for this comparison. Ratios show the fraction of  
292 models with correlations at the 90% confidence level, and p-values are based on the  
293 average correlation across models. Note the number of included stations varies depending  
294 on the availability of observed data (recall from Fig. 1 that a number of FLUXNET2015 sites  
295 do not allow for albedo estimations) and among models depending on whether the  
296 corresponding grid box is water or land. Furthermore, the data saved from the free-  
297 running ECMWF model simulations (EC) do not allow for estimation of albedo, so 11  
298 models are compared for albedo.

299 Unsurprisingly, we find surface net radiation errors correlate strongly to albedo errors,  
300 with 11 of 11 models registering significant correlations (two-tailed p-values  $< 0.05$ ) and  
301 the multi-model average correlation across 114-118 sites has a p-value of  $4 \times 10^{-7}$ . For net  
302 radiation versus precipitation, only 2 of 12 models (CL and M1) show significant  
303 correlation across 144-151 sites and p=0.55 for the multi-model average, so no direct  
304 arrow is drawn in Fig. 5. Note that precipitation errors arise not only from  
305 misrepresentation of land-atmosphere interactions, but also from the parameterization of  
306 dynamic and thermodynamic processes (so-called “model physics”) in the GCM.

307 FLUXNET2015 reports both raw and Bowen-ratio corrected heat fluxes. Corrected fluxes  
308 are available at fewer than 100 of the sites (two-tailed  $p=0.05$  for correlations  $|r| \geq 0.2$ ,  
309 compared to  $|r| \geq 0.16$  for the full set of sites), but generally correspond better to the  
310 models than uncorrected fluxes, which do not close the surface energy balance (cf. Figs. S9-  
311 S12). Regardless, the same story emerges with either set of fluxes: precipitation errors  
312 correlate significantly to latent heat flux errors ( $p=0.02$  in Fig. 5) but not sensible heat flux  
313 errors ( $p=0.31$ ). Meanwhile, albedo errors are very strongly linked to sensible heat flux  
314 errors ( $p=7 \times 10^{-5}$ ) but not latent heat flux errors ( $p=0.69$ ). Evaporative fraction (EF; the  
315 fraction of sensible + latent heat flux accounted for by the latent heat flux) relates strongly  
316 to both, but more strongly to errors in albedo ( $p=0.003$ ) than precipitation ( $p=0.05$ ).  
317 Consistently, correlating EF errors to the heat flux errors (black two-way arrows)  
318 demonstrates more variance explained by sensible heat flux than latent heat flux. Finally,  
319 LCL errors relate strongly to precipitation errors ( $p=2 \times 10^{-5}$ ) but are marginally significant  
320 in relation to albedo errors ( $p=0.06$ ). LCL has a prevalent negative bias (Fig. S8) reflecting  
321 the positive biases in specific humidity.

322 This analysis shows that models have troublesome errors in both the surface water and  
323 energy cycles, which make their way into the land-atmosphere coupling process chain. As a  
324 result, the degree to which weather and climate models correctly simulate feedbacks of  
325 land surface anomalies onto the atmosphere may be cast into some doubt. However, the  
326 origins of several sources of error have been identified and their alleviation can be  
327 pursued. In section 5 we will examine directly model fidelity in simulating metrics of land-  
328 atmosphere coupling.

329

330 **4. Mean Annual Cycle**

331 The next criterion for models, beyond simulating the annual means among  
332 FLUXNET2015 sites, is reproducing the annual cycle. The first harmonic is fit to the 12  
333 monthly means for each variable, determining phase and magnitude (half of valley-to-peak  
334 distance) using a standard Fourier transform. Errors in phase and magnitude at each  
335 station, quantified across all stations with similar metrics as the annual mean, indicate skill  
336 in simulating the annual cycle. Amplitude errors are displayed in conventional scatter  
337 diagrams (see Figs. S15-S24), but to display information for phase errors, we have  
338 configured the classical scatter diagram in a polar projection (see Figs. S25-34; the caption  
339 of Fig. S25 gives a detailed description of those plots). The whiskers in the supplemental  
340 figures again show models frequently display a smaller range of year-to-year variability  
341 than data from FLUXNET2015 sites. This may be partially explained by the scale difference  
342 (point measurements will vary more than grid-box averages) but is also likely due to the  
343 overly deterministic nature of many model parameterizations (Palmer 2012).

344 Taylor diagrams summarize the results across models. We focus on depictions of energy  
345 budget terms, as they reveal some of the main issues among models. Figure 6 shows model  
346 performance in simulating the amplitudes of the annual cycles of net radiation, sensible  
347 and latent heat fluxes across FLUXNET2015 sites. All model products demonstrate similar  
348 skill for net radiation, clustered between 0.64-0.78 correlation and a tendency toward too  
349 large an annual cycle. Only the offline NCEP and coupled ECMWF models have a negative  
350 bias in amplitude. Latent heat flux simulations show lower skill for every model, clustering  
351 between 0.28-0.43 for correlations. At the stations where energy balance corrected fluxes  
352 are provided, correlations improve to 0.37-0.50 (not shown). The positive bias is not so  
353 pervasive for latent heat; rather it appears the positive bias in net radiation tends to be  
354 expressed in the sensible heat term. There is also a much larger spread among models for

355 sensible heat, both in terms of correlation (0.14-0.54) and normalized standard deviation  
356 (0.78-1.50).

357 The models' skill in representing the phase of the annual cycle has a similar distribution  
358 (Fig. 7). The phase of net radiation is best represented, latent and sensible heat have spatial  
359 correlations of phasing between ~0.8-0.92 with sensible heat phases having slightly lower  
360 fidelity in general. It is interesting as the general consensus is that sensible heat flux is a  
361 simpler process to model than latent heat flux, yet it has been shown in other contexts that  
362 LSMs struggle more to simulate sensible heat flux (e.g., Best et al. 2015).

363 The Taylor diagram for the annual cycle of albedo (Fig. 8) shows very similar  
364 correlations of the yearly amplitude between models and observations (0.50-0.71) but a  
365 large range in standard deviation; Noah v2.7.1 (NL) shows a particularly high value  
366 contributing to large RMSE. The phase is better represented by all models, but interestingly  
367 the standard deviations are uniformly over-estimated. Most models now use global MODIS-  
368 based data sets of albedo as either a parameter set or for calibration of surface radiative  
369 parameterizations, so the large inter-model spread and lack of obvious clustering within  
370 families of models is surprising.

371

## 372 **5. Coupling Metrics**

373 Correlations between land surface state variables and surface fluxes (the terrestrial leg  
374 of coupling) and between land surface fluxes and atmospheric states or properties  
375 (atmospheric leg) may indicate feedbacks. For instance in the terrestrial leg, positive  
376 (negative) correlation between soil moisture and latent (sensible) heat flux implies soil  
377 moisture control of fluxes (a moisture limited situation) as opposed to energy (net  
378 radiation) limited situations where atmospheric states control the fluxes. However, the

379 variance in the driving term(s) must also be sufficiently large for a sensitivity of  
380 atmosphere to the land to have a consequential impact on climate, relative to other factors.

381 A coupling index  $I$  can be constructed from terms in either leg:  $I = \sigma(b)r(a,b) = \sigma(a)\frac{db}{da}$   
382 where  $a$  is the forcing and  $b$  is the responding variable,  $\sigma$  is standard deviation in time,  $r$  is  
383 correlation in time, and the linear regression slope of  $b$  on  $a$  is a measure of the sensitivity  
384 of  $b$  to  $a$  (Dirmeyer 2011, Dirmeyer et al. 2013).

385 Figure 9 synthesizes the performance of the various model configurations regarding  
386 two-legged coupling metrics linking soil moisture to boundary layer properties. The  
387 formulae for the coupling indices are indicated on the figure axes calculated from daily  
388 mean values. The terrestrial leg quantifies the combined sensitivity (correlation) of surface  
389 fluxes (here, latent heat flux) to land states (soil moisture) with variability (standard  
390 deviation) of the flux. The atmospheric leg links surface fluxes (sensible heat flux) to  
391 atmospheric states (LCL, which combines near surface temperature and humidity  
392 information). Larger values denote stronger feedback linkages.

393 In each panel of Fig. 9, similar to the approach of Sippel et al. (2017), quantities are  
394 calculated for the three consecutive months that have the warmest average temperature  
395 according to the FLUXNET2015 data. We distinguish between positive values of each  
396 metric, which indicate the existence of feedbacks from land to atmosphere, from negative  
397 (no feedbacks) by coloring the four quadrants by their coupling regimes: red = both legs  
398 present and a full coupling pathway; green = the land leg is present, the atmospheric leg is  
399 missing; blue = atmospheric leg is present, land is missing; grey = neither leg present. The  
400 white dots show where FLUXNET2015 sites fall in this two-dimensional metric space. The  
401 colored dots are each model's rendering of the metrics for the grid boxes containing the  
402 FLUXNET2015 sites; the color indicates the quadrant according to the FLUXNET

403 measurements. Thus, the more colored dots that fall in the quadrant with the matching  
404 color, the better the model is reproducing the global pattern of coupling regimes.

405 The model centroid usually lies below and to the right of the observed centroid for a  
406 given coupling regime, meaning models tend to over-estimate the terrestrial coupling index  
407 (the rightward offset), yet underestimate the strength of the atmospheric leg (the  
408 downward offset). Recall the number of FLUXNET2015 sites compared is not the same for  
409 each model. The percentage in each quadrant indicates how many of the FLUXNET2015  
410 sites in that regime are correctly placed in the right quadrant. For instance, the CFS  
411 Reanalysis has 76% of the FLUXNET stations exhibiting both coupling legs (red) in the  
412 correct regime. However, there are clearly many dots of other colors also in the red  
413 quadrant, showing the model places many other stations erroneously in that regime.  
414 Interestingly, none of the models put the few sites with no warm-season coupling in the  
415 grey quadrant. Overall, the reanalyses perform best: a 56.5% overall hit rate for the fully-  
416 coupled regime versus 52.8 for coupled models, and 44.0% for offline LSMs; and for the  
417 atmosphere-only coupling regime 49.2% versus 33.0% for coupled models and 31.6% for  
418 offline LSMs.

419 We have also examined performance of the models for their simulation of the observed  
420 FLUXNET2015 correlations and standard deviations (the two terms in the coupling  
421 indices) separately. As implied previously for the terrestrial leg, there is a positive bias in  
422 correlations for all models except for ERA-Interim (Table 2). Bias in the standard deviation  
423 of latent heat fluxes across all sites is small for most models, so most of the positive bias in  
424 coupling index comes from the correlation term. The model biases are even stronger in the  
425 anti-correlation between soil moisture and sensible heat flux (not shown). However, there  
426 is generally an even greater bias in correlations for the atmospheric leg (Table 2) paired in

427 every model with an underrepresentation of the daily variability of the LCL. These two  
428 biases compound, leading to the strong underrepresentation of coupling in the atmospheric  
429 leg of land-atmosphere interactions.

430 There are several caveats to note. First, the notion of calculating the atmospheric  
431 coupling leg from offline LSM simulations is only partially justifiable. It is certainly possible  
432 to calculate the correlations between surface fluxes and LCL height (which depends on  
433 near-surface meteorological data supplied as forcing to the LSM), but there is no possibility  
434 for the fluxes to affect 2m temperature or humidity. Thus, this is more of a test of model  
435 consistency than a true diagnosis of coupling.

436 Second, estimates of the correlation component of the coupling indices from observed  
437 data must be closer to zero than the true values in nature, because random measurement  
438 errors will degrade correlations (Robock et al. 1995). Thus, it is not necessarily wrong that  
439 models show a stronger terrestrial coupling leg than FLUXNET2015 data. The degree of  
440 impact can be estimated for variables such as soil moisture, whose auto-correlation time  
441 scales are much longer than the daily data interval (cf. Dirmeyer et al. 2016) but can be  
442 difficult to estimate from small samples or for other quantities. Nevertheless, the fact that  
443 models routinely underestimate the strength of the atmospheric leg runs counter to being  
444 attributable to random observational errors at FLUXNET sites, and likely represents real  
445 model bias.

446 Finally, the difference in scale between flux tower measurements (typically  
447 representative of conditions in an area of a square kilometer or less) and model grid-box  
448 averages (here ranging from  $200\text{--}2\times10^4\text{ km}^{-2}$ ) can affect statistics. Dirmeyer et al. (2016)  
449 showed there was little sensitivity of estimates of temporal variations in daily soil moisture  
450 to spatial scale differences in the model grid box range, however, the same may not be true

451 for other terms, or for correlations. The larger the averaging area, the smoother we should  
452 expect time series to be, potentially affecting estimation of coupling indices.

453

454 **6. Discussion and Summary**

455 We have confronted four different global model systems in multiple configurations (LSM  
456 only, LSM coupled to GCM, and reanalysis) with flux tower observations from 166 sites in  
457 the global FLUXNET2015 data set to determine how well they reproduce the spatial  
458 distribution of annual means and the annual cycle of state variables and terrestrial surface  
459 fluxes, and coupling indices between land and atmosphere. Returning to Table 2, there is a  
460 separation evident between the three classes of models. For the terrestrial leg of land-  
461 atmosphere coupling, all models appear to overestimate correlations between soil  
462 moisture and latent heat flux, with the caveat discussed previously that correlations  
463 necessarily skew low when calculated from observed data. Nevertheless, assuming as much  
464 as a 50% reduction from true correlations, it appears the reanalyses do the best job at  
465 reproducing observed correlations, followed by the free-running models and last the  
466 uncoupled LSMs. There is a similar stratification for the standard deviation of latent heat  
467 flux: reanalyses very closely represent the observed temporal variability of this flux, while  
468 coupled models and stand-alone LSMs progressively underestimate it. For the atmospheric  
469 leg, represented by the coupling index between sensible heat flux and LCL height, all  
470 classes of models severely underestimate the correlation and the day-to-day variability in  
471 the LCL. Reanalyses again do the best job at correlations and stand-alone LSMs are the  
472 worst. Here, coupled models fare slightly better than reanalyses in representing LCL  
473 variance. Given that reanalyses are somewhat constrained by the assimilation of  
474 observations, the errors in those models do not manifest as freely, so it makes sense

475 reanalyses should verify the best. On the other hand, offline LSMs lack some of the coupling  
476 we are trying to gauge. For example, surface sensible and latent heat fluxes cannot affect  
477 near surface temperature and humidity in such a configuration. This prescription of near-  
478 surface states interferes with the feedback processes.

479 General characteristics of note are that scatter diagrams of model versus FLUXNET2015  
480 quantities almost always show a linear regression slope indicating a wider range of  
481 variation in the observations. Models also tend to have lower interannual variability  
482 (length of whiskers) than observations suggest. These traits are consistent with scale  
483 differences between model grid cells and the area sampled by flux towers; model grid  
484 values represent areas at least 2-4 orders of magnitude larger, which particularly affects  
485 precipitation forcing. Thus, this difference is not a concern regarding model performance  
486 *per se*, but rather representativeness across scales.

487 Another general characteristic is that the models verify better against the corrected  
488 surface fluxes and quantities derived from them; wherein observed sensible and latent heat  
489 values are adjusted to close the surface energy budget. This makes sense as models close  
490 surface energy (and water) budgets by design, whereas closure is not assured in an  
491 observational setting where a number of instruments, with different calibrations and error  
492 characteristics, contribute separate terms of the surface balances. However, when the  
493 propagation of model errors through the energy and water cycles are traced (Fig. 5), EF in  
494 models shows strong sensitivity to radiation errors, implying that conservation of Bowen  
495 ratio (and thus EF) as a means to correct observed heat fluxes and close the energy balance  
496 may not be the most efficacious.

497 There are differences that do appear to reflect general model biases. All models and  
498 configurations show a positive bias in near-surface humidity (Fig. S3, S14), downward

499 shortwave radiation (Figs. S4, S17) and a range of biases in downward longwave radiation  
500 (Fig. S5). Such radiation biases are a long-standing problem in global models (cf. Dirmeyer  
501 et al. 2006), and stem from problems in the parameterization of atmospheric radiative  
502 transfer, clouds and aerosols in GCMs. However, not all radiative errors are atmospheric in  
503 origin – there is clear indication that LSMs struggle to represent the spatial and temporal  
504 variability of surface albedo (Figs. 4, 8).

505 Combined with well-known difficulties models have in simulating precipitation (Figs. 2,  
506 S6, S15, S25), it becomes extremely challenging for models to partition available energy  
507 correctly at the surface between latent, sensible and ground heat fluxes, and to reproduce  
508 the spatiotemporal patterns of relationships between soil moisture, surface fluxes and the  
509 lower troposphere. Errors in latent heat flux generally correlate significantly to  
510 precipitation errors, while sensible heat flux errors relate strongly to surface albedo errors.  
511 Evaporative fraction errors connect to both, but more strongly to the energy (albedo –  
512 sensible heat flux) pathway than the water (precipitation – latent heat flux) pathway.  
513 Height of the LCL, which has a strong negative bias across all models related to the positive  
514 humidity bias, has errors that correlate strongly to the water cycle pathway, but also to the  
515 energy cycle pathway.

516 The spatial distributions of the annual cycles are generally well reproduced for energy  
517 budget terms, except for upward shortwave radiation, related to the albedo problems  
518 discussed earlier. However, there is a tendency for too strong a seasonal cycle in net  
519 radiation, caused by excessive summertime downward shortwave radiation, and expressed  
520 more strongly in the annual cycle of sensible heat flux than latent heat flux. Models  
521 generally do very well representing the spatial distribution of the phasing of the annual

522 cycle, even for precipitation (64-92% of variance explained) and soil moisture (40-61% of  
523 variance explained).

524 Finally, despite the barriers described above to models' capacity to represent the  
525 spatiotemporal distribution of land-atmosphere coupling, we find models often do a  
526 reasonable job. Some systematic biases are evident: models consistently over-estimate the  
527 strength of the terrestrial leg of coupling (namely, too strong a correlation between soil  
528 moisture and sensible heat fluxes), yet even more clearly underestimate the strength of the  
529 atmospheric leg (both the correlation between surface fluxes and boundary layer  
530 properties, and day-to-day variability of boundary layer properties). Random  
531 observational error tends to reduce correlations between observed quantities, so it is  
532 possible that models are not greatly overestimating the terrestrial leg of coupling, or  
533 perhaps are not overestimating it at all. However, we find the time series at most  
534 FLUXNET2015 sites are too short to robustly estimate the random error effects on  
535 correlation – perhaps in another ten years we will be able to quantify these errors.  
536 Similarly, the spatial scale differences between observations and model output may  
537 contribute to the variance differences in the atmospheric leg, but disparity in correlations  
538 between surface fluxes and LCL could only be stronger than calculated here, not weaker,  
539 because of the effect of measurement error.

540 LSMs forced by global gridded meteorology rather than local forcing from the tower  
541 sites themselves are handicapped to some degree (cf. Chen et al. 2017). So our most  
542 confident conclusion regarding land-atmosphere coupling is that models under-represent  
543 the feedback of surface fluxes on boundary layer properties at FLUXNET2015 sites. We find  
544 this unique data set has potential for model development and parameter optimization to

545 alleviate biases in model configurations shown to mirror those used in forecasting  
546 applications (Orth et al. 2016, 2017).

547 Overall, we conclude that many of the long-known problems and biases in global models  
548 of the land-atmosphere portion of the climate system still exist. Nevertheless, there is a fair  
549 degree of compensation among errors, such that model representations of land-  
550 atmosphere coupling often appear fairly good. Some targets for model improvement are  
551 clear, however, as coupling linkages suggest processes where problems may lie. The  
552 representation of surface albedo (LSM) and the quantities of downward radiation at the  
553 surface (GCM) need improvement among the energy cycle terms, along with the  
554 partitioning of available energy between latent and sensible heat flux (a coupled model  
555 development problem). Precipitation errors remain large, and inconsistencies in  
556 representing soil moisture among models and between models and nature (cf. Koster et al.  
557 2009) remain stubborn issues.

558 As one might expect, reanalyses tend to perform better, as they are more constrained by  
559 observational data. LSMS run offline also benefit from meteorological forcing that is highly  
560 observational in origin, but can be handicapped by their lack of two-way interaction with  
561 the lower troposphere. It should be clear from the various figures that individual models  
562 perform better or worse at simulating specific facets of land-atmosphere interactions.  
563 However, we emphasize here the commonalities among models more than differences. This  
564 study is not primarily intended as a model inter-comparison, but rather a multi-model  
565 attempt to draw model-independent conclusions about the current state of performance of  
566 land-atmosphere models (in various configurations) by confronting them with a new and  
567 unique observational data set.

568 Furthermore, this study is not a final judgement, but a first look that will hopefully  
569 catalyze accelerated development and improvement in coupled land-atmosphere modeling.  
570 Application of cross-component metrics like coupling indices can reveal prime areas for  
571 model development that are not evident from piecewise evaluation of model components.  
572 The next step is intensive, focused sensitivity studies with individual models, preferably  
573 validated in the context of coupled model systems, that will zero in on the problematic  
574 parameterizations. We may also need to revisit some of the fundamental assumptions that  
575 underpin the formulations in models (e.g., Cheng et al. 2017).

576 Furthermore, it is clear that long-term observational monitoring is highly valuable, and  
577 that value only increases with the duration of data sets at individual sites. Greater spatial  
578 distribution of flux tower sites, especially into under-monitored regions outside middle-  
579 and high-latitudes, would further increase the overall usefulness to model development.

580

581 *Acknowledgments:* This work has been primarily supported by National Aeronautics and  
582 Space Administration grant NNX13AQ21G. NCAR model simulations were conducted with  
583 support from the National Science Foundation grant AGS-1419445. The ERA-Interim  
584 reanalysis data are provided by ECMWF and processed by LSCE. This work uses eddy  
585 covariance data acquired and shared by the FLUXNET community (listed in Table S1),  
586 including these networks: AmeriFlux, AfriFlux, AsiaFlux, CarboAfrica, CarboEuropeIP,  
587 CarboItaly, CarboMont, ChinaFlux, Fluxnet-Canada, GreenGrass, ICOS, KoFlux, LBA, NECC,  
588 OzFlux-TERN, TCOS-Siberia, and USCCC. The FLUXNET eddy covariance data processing  
589 and harmonization was carried out by the European Fluxes Database Cluster, AmeriFlux  
590 Management Project, and Fluxdata project of FLUXNET, with the support of CDIAC and  
591 ICOS Ecosystem Thematic Center, and the OzFlux, ChinaFlux and AsiaFlux offices. Taylor

592 diagrams were produced using a modified version of the GrADS script developed by Bin  
593 Guan. We thank Cristina Benzo for her contributions to produce Table S1, and Eleanor  
594 Blyth and two anonymous reviewers for their helpful review comments.

595

596 **References:**

597 Andreae, M. O., and co-authors, 2002: Biogeochemical cycling of carbon, water, energy,  
598 trace gases, and aerosols in Amazonia: The LBA-EUSTACH experiments. *J. Geophys. Res.*,  
599 **107**, LBA33-1-LBA33-25.

600 Baldocchi, D., and co-authors, 2001: FLUXNET: A new tool to study the temporal and spatial  
601 variability of ecosystem-scale carbon dioxide, water vapor and energy flux densities.  
602 *Bull. Amer. Meteor. Soc.*, **82**, 2415-2434.

603 Balsamo, G., and co-authors, 2015: ERA-Interim/Land: a global land surface reanalysis  
604 data set, *Hydrol. Earth Syst. Sci.*, **19**, 389- 407, doi: 10.5194/hess-19-389- 2015.

605 Balzarolo, M., and co-authors, 2014: Evaluating the potential of large-scale simulations to  
606 predict carbon fluxes of terrestrial ecosystems over a European Eddy Covariance  
607 network, *Biogeosci.*, **11**, 2661-2678, doi:10.5194/bg-11-2661-2014.Best, M. J., and Co-  
608 authors, 2015: The plumbing of land surface models: benchmarking model performance.  
609 *J. Hydrometeor.*, **16**, 1425-1442, doi: 10.1175/JHM-D-14-0158.1.

610 Bonan, G. B., K. W. Oleson, R. A. Fisher, G. Lasslop, and M. Reichstein, 2012: Reconciling leaf  
611 physiological traits and canopy flux data: Use of the TRY and FLUXNET databases in the  
612 Community Land Model version 4, *J. Geophys. Res.*, **117**, G02026, doi:  
613 10.1029/2011JG001913.

614 Boussetta, S., G. Balsamo, A. Beljaars, T. Kral, L. Jarlan, 2013: Impact of a satellite-derived  
615 leaf area index monthly climatology in a global numerical weather prediction model. *Int.*  
616 *J. Remote Sens.*, **34**, 3520-3542. doi: 10.1080/01431161.2012.716543.

617 Chen, L., P. A. Dirmeyer, Z. Guo and N. M. Schultz, 2017: Pairing FLUXNET sites to validate  
618 model representations of land use/land cover change. *Hydrol. Earth Sys. Sci. Discus.*, doi:  
619 10.5194/hess-2017-190.

620 Cheng, Y., C. Sayde, Q. Li, J. Basara, J. Selker, E. Tanner, and P. Gentine, 2017: Failure of  
621 Taylor's hypothesis in the atmospheric surface layer and its correction for eddy-  
622 covariance measurements. *Geophys. Res. Lett.*, **44**, 4287-4295, doi:  
623 10.1002/2017GL073499.

624 Dee, D. P., and co-authors, 2011: The ERA-Interim reanalysis: configuration and  
625 performance of the data assimilation system. *Quart. J. Roy. Meteor. Soc.*, **137**, 553-597,  
626 doi: 10.1002/qj.828.

627 Dirmeyer, P. A., R. D. Koster, and Z. Guo, 2006: Do global models properly represent the  
628 feedback between land and atmosphere? *J. Hydrometeor.*, **7**, 1177-1198, doi:  
629 10.1175/JHM532.1.

630 Dirmeyer, P. A., 2011: The terrestrial segment of soil moisture-climate coupling. *Geophys.*  
631 *Res. Lett.*, **38**, L16702, doi: 10.1029/2011GL048268.

632 Dirmeyer, P. A., S. Kumar, M. J. Fennessy, E. L. Altshuler, T. DelSole, Z. Guo, B. Cash and D.  
633 Straus, 2013: Model estimates of land-driven predictability in a changing climate from  
634 CCSM4. *J. Climate*, **26**, 8495-8512, doi: 10.1175/JCLI-D-13-00029.1.

635 Dirmeyer, P. A., and co-authors, 2016: Confronting weather and climate models with  
636 observational data from soil moisture networks over the United States. *J. Hydrometeor.*,  
637 **17**, 1049-1067, doi: 10.1175/JHM-D-15-0196.1.

638 Dirmeyer, P. A., P. Gentine, M. B. Ek, and G. Balsamo, 2017: Land Surface Processes Relevant  
639 to S2S Prediction. [Chapter 8 in: *The Gap Between Weather and Climate Forecasting:*  
640 *Sub-Seasonal to Seasonal Prediction* (A. W. Robertson and F. Vitart Eds.)], Elsevier, (in  
641 revision).

642 Dorigo, W. A., and co-authors, 2011: The International Soil Moisture Network: a data  
643 hosting facility for global in situ soil moisture measurements, *Hydrol. Earth Syst. Sci.*, **15**,  
644 1675-1698, doi: 10.5194/hess-15-1675-2011.

645 Dorigo, W.A., and co-authors, 2013: Global automated quality control of in situ soil  
646 moisture data from the International Soil Moisture Network. *Vadose Zone J.*, **12**(3), doi:  
647 10.2136/vzj2012.0097.

648 Dorigo, W., and co-authors, 2017: ESA CCI Soil Moisture for improved Earth system  
649 understanding: state-of-the art and future directions, *Remote Sens. Env.* (in press),  
650 10.1016/j.rse.2017.07.001.

651 Ek, M. B., K. E. Mitchell, Y. Lin, E. Rogers, P. Grunmann, V. Koren, G. Gayno, and J. D. Tarplay,  
652 2003: Implementation of Noah land surface model advances in the National Centers for  
653 Environmental Prediction operational mesoscale Eta model. *J. Geophys. Res.*, **108**, 8851,  
654 doi: 10.1029/2002JD003296.

655 Famiglietti, J. S., J. A. Devereaux, C. A. Laymon, T. Tsegaye, P. R. Houser, T. J. Jackson, S. T.  
656 Graham, M. Rodell, and P. J. van Oevelen, 1999: Ground-based investigation of soil  
657 moisture variability within remote sensing footprints during the Southern Great Plains  
658 97 (SGP97) hydrology experiment. *Water Resour. Res.*, **35**, 1839-1851.

659 Gelaro, R., and co-authors, 2017: The Modern-Era Retrospective analysis for Research and  
660 Applications, version 2 (MERRA-2). *J. Climate*, **30**, 5419-5454, doi: 10.1175/JCLI-D-16-  
661 0758.1.

662 Global Modeling and Assimilation Office (GMAO), 2015: MERRA-2 inst1\_2d\_lfo\_Nx: 2d, 1-  
663 Hourly, Instantaneous, Single-Level, Assimilation, Land Surface Forcings V5.12.4,  
664 Greenbelt, MD, USA, Goddard Earth Sciences Data and Information Services Center (GES  
665 DISC), Accessed 3 July 2016, doi: 10.5067/RCMZA6TL70BG.

666 Global Modeling and Assimilation Office (GMAO), 2015: MERRA-2 tavg1\_2d\_lfo\_Nx: 2d, 1-  
667 Hourly, Time-Averaged, Single-Level, Assimilation ,Land Surface Forcings V5.12.4,  
668 Greenbelt, MD, USA, Goddard Earth Sciences Data and Information Services Center (GES  
669 DISC), Accessed 3 July 2016, doi: 10.5067/L0T5GEG1NYFA.

670 Jackson, T. J., and A. Y. Hsu, 2001: Soil moisture and TRMM microwave imager relationships  
671 in the Southern Great Plains 1999 (SGP99) experiment, IEEE Trans. *Geosci. Remote  
672 Sens.*, **39**, 1632-1642.

673 Kinter III, J. L., and co-authors, 2013: Revolutionizing climate modeling – Project Athena: A  
674 multi-institutional, international collaboration. *Bull. Amer. Meteor. Soc.*, **94**, 231-245,  
675 doi: 10.1175/BAMS-D-11-00043.1.

676 Koster, R. D., Z. Guo, P. A. Dirmeyer, R. Yang, K. Mitchell, and M. J. Puma, 2009: On the nature  
677 of soil moisture in land surface models. *J. Climate*, **22**, 4322-4335, doi:  
678 10.1175/2009JCLI2832.1.

679 Lawrence, D. M., and co-authors, 2011: Parameterization improvements and functional and  
680 structural advances in version 4 of the Community Land Model. *J. Adv. Model. Earth*  
681 *Syst.*, **3**, doi: 10.1029/2011MS000045.

682 Mahanama, S. P. P., R. D. Koster, G. K. Walker, L. L. Takacs, R. H. Reichle, G. De Lannoy, Q. Liu,  
683 B. Zhao, and M. J. Suarez, 2015: Land Boundary Conditions for the Goddard Earth  
684 Observing System Model Version 5 (GEOS-5) Climate Modeling System - Recent Updates  
685 and Data File Descriptions. NASA/TM-2015-104606, Vol. 39, 55 pp. Document (4608  
686 kB).

687 Melaas, E. K., A. D. Richardson, M. A. Friedl, D. Dragoni, C. M. Gough, M. Herbst, L.  
688 Montagnani, and E. Moors, 2013: Using FLUXNET data to improve models of springtime  
689 vegetation activity onset in forest ecosystems. *Ag. Forest Meteor.*, **171-172**, 46-56.

690 Mitchell, K., 2005: The Community Noah Land Surface Model User's Guide Public Release  
691 Version 2.7.1, [available at:  
692 [http://www.ral.ucar.edu/research/land/technology/lsm/noah/Noah\\_LSM\\_USERGUIDE\\_2.7.1.pdf](http://www.ral.ucar.edu/research/land/technology/lsm/noah/Noah_LSM_USERGUIDE_2.7.1.pdf)].

693

694 Molod, A., Takacs, L., Suarez, M., and Bacmeister, J., 2015: Development of the GEOS-5  
695 atmospheric general circulation model: evolution from MERRA to MERRA2, *Geosci.  
696 Model Dev.*, **8**, 1339-1356, doi: 10.5194/gmd-8-1339-2015.

697 Orth, R., E. Dutra, and F. Pappenberger, 2016: Improving weather predictability by  
698 including land surface model parameter uncertainty. *Mon. Wea. Rev.*, **144**, 1551–1569,  
699 doi: 10.1175/MWR-D-15-0283.1.

700 Orth, R., Dutra, E., Trigo, I. F., and Balsamo, G., 2017: Advancing land surface model  
701 development with satellite-based Earth observations, *Hydrol. Earth Syst. Sci.*, **21**, 2483-  
702 2495, doi:10.5194/hess-21-2483-2017.

703 Palmer, T. N., 2012: Towards the probabilistic Earth-system simulator: a vision for the  
704 future of climate and weather prediction. *Quart. J. Roy. Meteor. Soc.*, **138**, 841-861.

705 Pastorello, G. Z., D. Papale, H. Chu, C. Trotta, D. A. Agarwal, E. Canfora, D. D. Baldocchi, and  
706 M. S. Torn, 2017: A new data set monitors land-air exchanges. *EOS Earth & Space Science*  
707 *News*, **98**(8), 28-32.

708 Peters-Lidard, C. D., and co-authors, 2007: High performance earth system modeling with  
709 NASA/GSFC's Land Information System. *Innov. Syst. Software Eng.*, **3**, doi:  
710 10.1007/s11334-007-0028-x.

711 Purdy, A. J., J. B. Fisher, M. L. Goulden, and J. S. Famiglietti, 2016. Ground heat flux: An  
712 analytical review of 6 models evaluated at 88 sites and globally. *J. Geophys. Res.*, **121**,  
713 3045-3059.

714 Quiring, S. M., T. W. Ford, J. K. Wang, A. Khong, E. Harris, T. Lindgren, D. W. Goldberg, and Z.  
715 Li, 2016: North American Soil Moisture Database: Development and applications. *Bull.*  
716 *Amer. Meteor. Soc.*, **97**, 1441-1460.

717 Reichle, R. H., and Q. Liu, 2014. Observation-Corrected Precipitation Estimates in GEOS-5.  
718 NASA/TM-2014-104606, Vol. 35. <http://gmao.gsfc.nasa.gov/pubs/docs/Reichle734.pdf>.

719 Reichle, R. H., C. S. Draper, Q. Liu, M. Girotto, S. P. Mahanama, R. D. Koster, and G. De Lannoy,  
720 2017a. Assessment of MERRA-2 land surface hydrology estimates. *J. Climate*, **30**, 2937-  
721 2960, doi: 10.1175/JCLI-D-16-0720.1.

722 Reichle, R., Q. Liu, R. Koster, C. Draper, S. Mahanama, and G. Partyka, 2017b. Land surface  
723 precipitation in MERRA-2. *J. Climate*, **30**, 1643-1664, doi: 10.1175/JCLI-D-16-0570.1.

724 Reichstein, M., and co-authors, 2005: On the separation of net ecosystem exchange into  
725 assimilation and ecosystem respiration: review and improved algorithm. *Glob. Change*  
726 *Biol.*, **11**, 1424-1439, doi: 10.1111/j.1365-2486.2005.001002.x.

727 Rienecker, M. M., and co-authors, 2011: MERRA: NASA's Modern-Era Retrospective  
728 Analysis for Research and Applications. *J. Climate*, **24**, 3624-3648, doi:10.1175/JCLI-D-  
729 11-00015.1.

730 Robock, A., K. Ya. Vinnikov, C. A. Schlosser, N. A. Speranskaya and Y. Xue, 1995: Use of  
731 midlatitude soil moisture and meteorological observations to validate soil moisture  
732 simulations with biosphere and bucket models.. *J. Climate*, **8**, 15-35.

733 Saha, S., and co-authors, 2010: The NCEP Climate Forecast System Reanalysis. *Bull. Amer.*  
734 *Meteor. Soc.*, **91**, 1015–1057, doi: 10.1175/2010BAMS3001.1.

735 Santanello, J. A., C. D. Peters-Lidard, and S. V. Kumar, 2011: Diagnosing the sensitivity of  
736 local land-atmosphere coupling via the soil moisture-boundary layer interaction. *J.*  
737 *Hydrometeor.*, **12**, 766-786.

738 Santanello, J. A., P. A. Dirmeyer, C. R. Ferguson, K. L. Findell, A. B. Tawfik, A. Berg, M. B. Ek, P.  
739 Gentine, B. Guillod, C. van Heerwaarden, J. Roundy, and V. Wulfmeyer, 2017: Land-  
740 atmosphere interactions: The LoCo perspective. *Bull. Amer. Meteor. Soc.*, (in revision).

741 Sellers, P. J., F. G. Hall, G. Asrar, D. E. Strelbel, and R. E. Murphy, 1992: An overview of the  
742 First International Satellite Land Surface Climatology Project (ISLSCP) Field Experiment  
743 (FIFE). *J. Geophys. Res.*, **97**, 18,345-18,372.

744 Sellers, P. J., and co-authors, 1995: The Boreal Ecosystem-Atmosphere Study (BOREAS): An  
745 overview and early results from the 1994 field year. *Bull. Amer. Meteor. Soc.*, **76**, 1549-  
746 1577.

747 Sheffield, J., G. Goteti, and E. F. Wood, 2006: Development of a 50-yr high-resolution global  
748 dataset of meteorological forcings for land surface modeling. *J. Climate*, **19**, 3088-3111.

749 Shukla, R. P., B. Huang, L. Marx, J. L. Kinter and C.-S. Shin, 2017: Predictability and  
750 prediction of Indian summer monsoon by CFSv2: implication of the initial shock effect.  
751 *Climate Dyn.* (published online), doi: 10.1007/s00382-017-3594-0.

752 Sippel, S., J. Zscheischler, M. D. Mahecha, R. Orth, M. Reichstein, M. Vogel, and S. I.  
753 Seneviratne, 2017: Refining multi-model projections of temperature extremes by  
754 evaluation against land-atmosphere coupling diagnostics. *Earth Sys. Dyn.*, **8**, 387-403.

755 Slater, A. G., 2016: Surface solar radiation in North America: A comparison of observations,  
756 reanalyses, satellite, and derived products. *J. Hydrometeor.*, **17**, 401-420.

757 Viovy, N., 2013. CRUNCEP data set for 1901–2010, [Available at  
758 <https://www.earthsystemgrid.org/dataset/ucar.cgd.ccsm4.CRUNCEP.v4.html>].

759 Vuichard, N., and D. Papale, 2015: Filling the gaps in meteorological continuous data  
760 measured at FLUXNET sites with ERA-Interim reanalysis. *Earth Sys. Sci. Data*, **7**, 157-  
761 171, doi: 10.5194/essd-7-157-2015.

762 Williams, M., and co-authors, 2009: Improving land surface models with FLUXNET data.  
763 *Biogeosci.* **6**, 1341-1359.

764 Xia, Y., and co-authors, 2012: Continental-scale water and energy flux analysis and  
765 validation for the North American Land Data Assimilation System project phase 2  
766 (NLDAS-2): 1. Intercomparison and application of model products, *J. Geophys. Res.*, **117**,  
767 D03109, doi:10.1029/2011JD016048.

768 Xie, P., and P. A. Arkin, 1997: Global precipitation: A 17-year monthly analysis based on  
769 gauge observations, satellite estimates, and numerical model outputs. *Bull. Amer.*  
770 *Meteor. Soc.*, **78**, 2539-2558.

771 Xie, P., M. Chen, A. Yatagai, T. Hayasaka, Y. Fukushima, and S. Yang, 2007: "A gauge-based  
772 analysis of daily precipitation over East Asia." *J. Hydrometeor*, **8**, 607-626.

773 Zaitchik, B., F., J. A. Santanello, S. V. Kumar, and C. D. Peters-Lidard, 2013: Representation of  
774 soil moisture feedbacks during drought in NASA Unified WRF (NU-WRF). *J.*  
775 *Hydrometeor*, **14**, 360-367.

776 Table 1. Specifications for the four land and atmosphere model systems, including time  
 777 span of data and spatial resolution. Two-letter abbreviations are used in subsequent  
 778 figures and tables; generally for the first letter: N=NCEP, M=NASA (MERRA system),  
 779 C=NCAR (Community models), E=ECMWF; for the second letter: L=LSM run “offline”,  
 780 C=LSM coupled to GCM, R=reanalysis (except that two MERRA reanalyses are included, so  
 781 they are labeled 1 and 2).

System	Offline LSM	Free-Running	Reanalysis
<b>NOAA/ NCEP</b>	<b>NL:</b> Noah2.7.1 [1982- 2010] $1^\circ \times 1^\circ$ with forcing from Sheffield et al. (2006)	<b>NC:</b> CFSv2 [48 years] $\sim 0.94^\circ \times 0.94^\circ$ fully coupled Shukla et al. (2017)	<b>NR:</b> CFSR [1979-2009] $0.31^\circ \times 0.37^\circ$ Saha et al. (2010)
<b>NASA/ GMAO</b>	<b>ML:</b> Catchment with boundary conditions from Mahanama et al (2015) plus physics changes [1980-2015] $0.625^\circ \times 0.5^\circ$ with MERRA-2 forcing and corrected precipitation Reichle et al. (2017b), GMAO (2015a,b)	<b>MC:</b> GEOS5 Heracles-5 4 p3-M3; LSM as in <b>ML</b> [2000-2015] $0.5^\circ \times 0.5^\circ$ with observed SST	<b>M2:</b> MERRA-2 [1980- 2015] $0.625^\circ \times 0.5^\circ$ Gelaro et al. (2017); <b>M1:</b> MERRA [1980- 2015] $0.667^\circ \times 0.5^\circ$ Rienecker et al (2011)
<b>NCAR</b>	<b>CL:</b> CLM4.5 [1991-2010] $1.25^\circ \times 0.9^\circ$ with CRUNCEP (Viovy 2013) forcing Lawrence et al. (2011)	<b>CC:</b> CESM 1.2.2 (CAM4 + CLM4.5) [1991- 2014] $1.25^\circ \times 0.9^\circ$ with climatological SST	--none--
<b>ECMWF</b>	<b>EL:</b> HTESSEL 43R1 [1979-2015] TCo639 16km Balsamo et al. (2015)	<b>EC:</b> IFS in Athena Project [1961-2007] T1279 interpolated to N80 $1.125^\circ \times 1.125^\circ$ with observed SST Kinter et al. (2013)	<b>ER:</b> ERA-Interim [1979-2015] $0.75^\circ \times 0.75^\circ$ Dee et al. (2011)

782  
 783

784 Table 2: The average value of the two terms used to calculate the terrestrial and  
 785 atmospheric coupling indices using data from FLUXNET2015, each model, and averages  
 786 from various groupings of the models.

787

	Terrestrial		Atmospheric	
	$r(\text{SM,LHF})$	$\sigma(\text{LHF})$	$r(\text{SHF,LCL})$	$\sigma(\text{LCL})$
FLUXNET2015	<b>0.07</b>	<b>21.2 Wm<sup>-2</sup></b>	<b>0.35</b>	<b>432 m</b>
NL	0.31	18.2	-0.22	221
NC	0.21	21.5	0.13	412
NR	0.22	23.1	0.21	396
ML	0.14	15.9	0.08	366
MC	0.13	14.0	0.02	291
M2	0.11	21.4	0.12	287
M1	0.21	22.1	0.18	340
CL	0.28	19.1	0.24	191
CC	0.18	24.1	0.15	357
EL	0.11	21.6	0.09	371
EC	0.19	17.7	0.08	350
ER	0.05	18.8	0.13	291
All	<b>0.18</b>	<b>19.8</b>	<b>0.10</b>	<b>323</b>
LSMs	0.21	18.7	0.05	287
Coupled	0.18	19.3	0.10	352
Reanalyses	0.15	21.4	0.16	328

788

789

790 **Figure Captions:**

791 Figure 1: Location of the FLUXNET2015 Tier-1 sites used in this study. Triangles indicate  
792 no upward shortwave radiation measurements available to estimate surface albedo,  
793 pluses mean no Bowen ratio corrected surface heat fluxes provided, exes indicate neither  
794 albedo nor corrected heat fluxes are available, circles have both. Color of the symbol  
795 indicates the length of data series available.

796 Figure 2: Scatter of annual total precipitation measurements at FLUXNET2015 sites  
797 (abscissa) to estimates (ordinate) from gridded observationally-based precipitation  
798 analyses (top two rows) or reanalyses constrained by data assimilation (bottom row)  
799 using the value from the grid box containing the FLUXNET2015 site location (unless data  
800 are missing or indicated to be an all-ocean grid box). Dash-dotted diagonal grey line  
801 indicates  $X=Y$ . Colors indicate years of available data from each FLUXNET2015 site,  
802 whiskers span range of annual totals from FLUXNET2015 (horizontal) or gridded  
803 estimates (vertical) for years where data sets overlap. Purple line is the best-fit linear  
804 regression of  $Y$  on  $X$ . Statistics are explained in the text.

805 Figure 3: Taylor diagram of annual mean surface radiation terms for the 12 indicated  
806 models verified against FLUXNET2015 sites for downward solar radiation (black),  
807 downward longwave radiation (red), upward shortwave radiation (blue) and net  
808 radiation (green). Dot colors indicate mean bias and size shows percentage of stations  
809 where the range of the annual totals from the model overlaps the span from  
810 FLUXNET2015 sites (also presented in tabular form in the upper right).

811 Figure 4: As in Fig. 3 for surface albedo; annual mean (black) and boreal summer (JJA)  
812 mean (red).

813 Figure 5: Propagation of errors estimated from their rank correlations among precipitation  
814 (P), height of the lifting condensation level (LCL), evaporative fraction (EF), sensible and  
815 latent heat flux (SH & LH), surface albedo ( $\alpha$ ) and net radiation ( $R_{Net}$ ) across  
816 FLUXNET2015 stations. Ratios show the number of models out of 11 (correlations  
817 involving  $\alpha$ ) or 12 (other variables) with p-values below 0.10; p-value shown is based on  
818 the average of correlations across all models. Widths of arrows follow significance of  
819 correlations and no arrows are drawn where p-values are large. The wide double arrows  
820 between EF and heat fluxes denote p-values  $< 10^{-12}$ .

821 Figure 6: As in Fig. 3 for the magnitude of the annual cycle (first harmonic calculated from  
822 monthly means) of sensible heat flux (orange), latent heat flux (cyan) and net radiation at  
823 the surface (green).

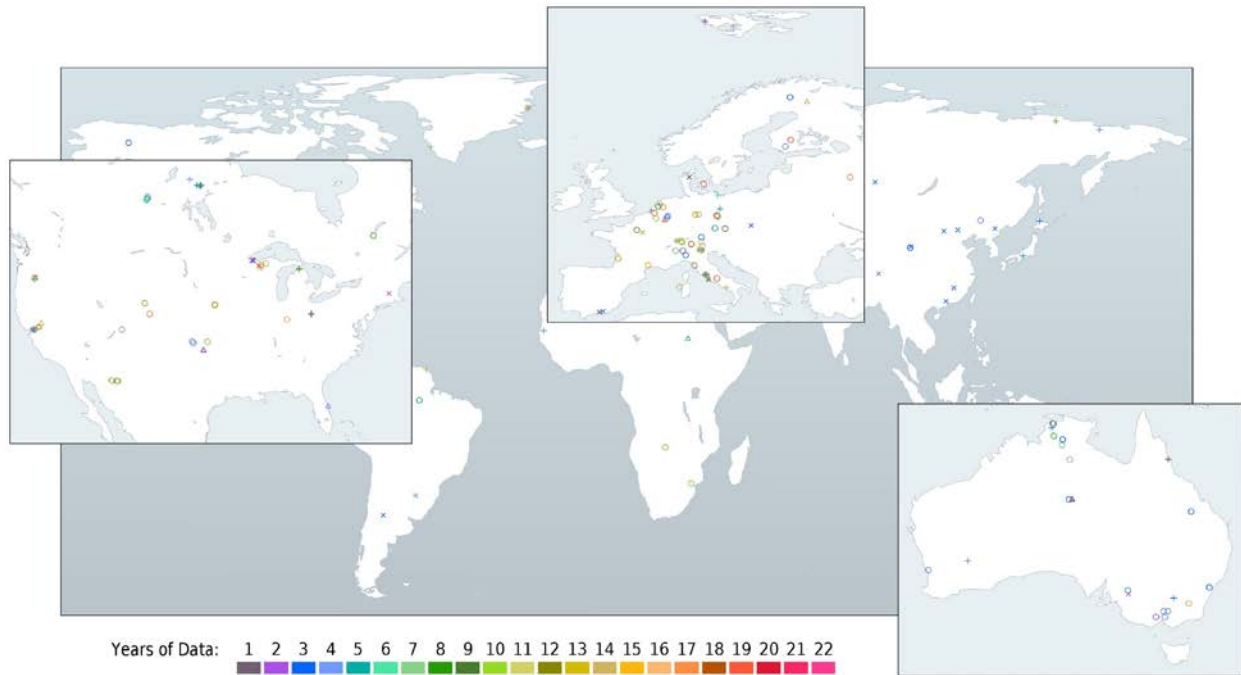
824 Figure 7: As in Fig. 6 for phase of the annual cycle of sensible heat flux (orange) and latent  
825 heat flux (cyan) and net radiation at the surface (green).

826 Figure 8: As in Fig. 6 for the magnitude (brown) and phase (purple) of the annual cycle of  
827 surface albedo.

828 Figure 9: Distribution of coupling indices for the terrestrial (x-axis) and atmospheric (y-  
829 axis) legs for the warmest consecutive 3 months of the annual cycle for FLUXNET2015  
830 sites (white dots; identical in each panel) and for each model as indicated. Colors of dots  
831 indicate in which quadrant that FLUXNET2015 site lies: red = both indices positive;  
832 green = terrestrial positive, atmospheric negative; blue = atmospheric positive,  
833 terrestrial negative; grey = both negative. The white circle indicates the centroid of all  
834 FLUXNET2015 stations that are in that quadrant, connected by a colored dotted line to a  
835 colored circle that is the centroid of the same stations' corresponding grid boxes as  
836 simulated by the model. Numbers in the corners of each quadrant show the number of

837 points in that quadrant according to the model and FLUXNET2015 data, separated by a  
838 colon, and the percentage of the FLUXNET2015 sites within that quadrant that the model  
839 placed in the same quadrant. The percentage in red at the upper right of each panel is the  
840 overall percentage of sites where model and FLUXNET2015 agree on the quadrant.

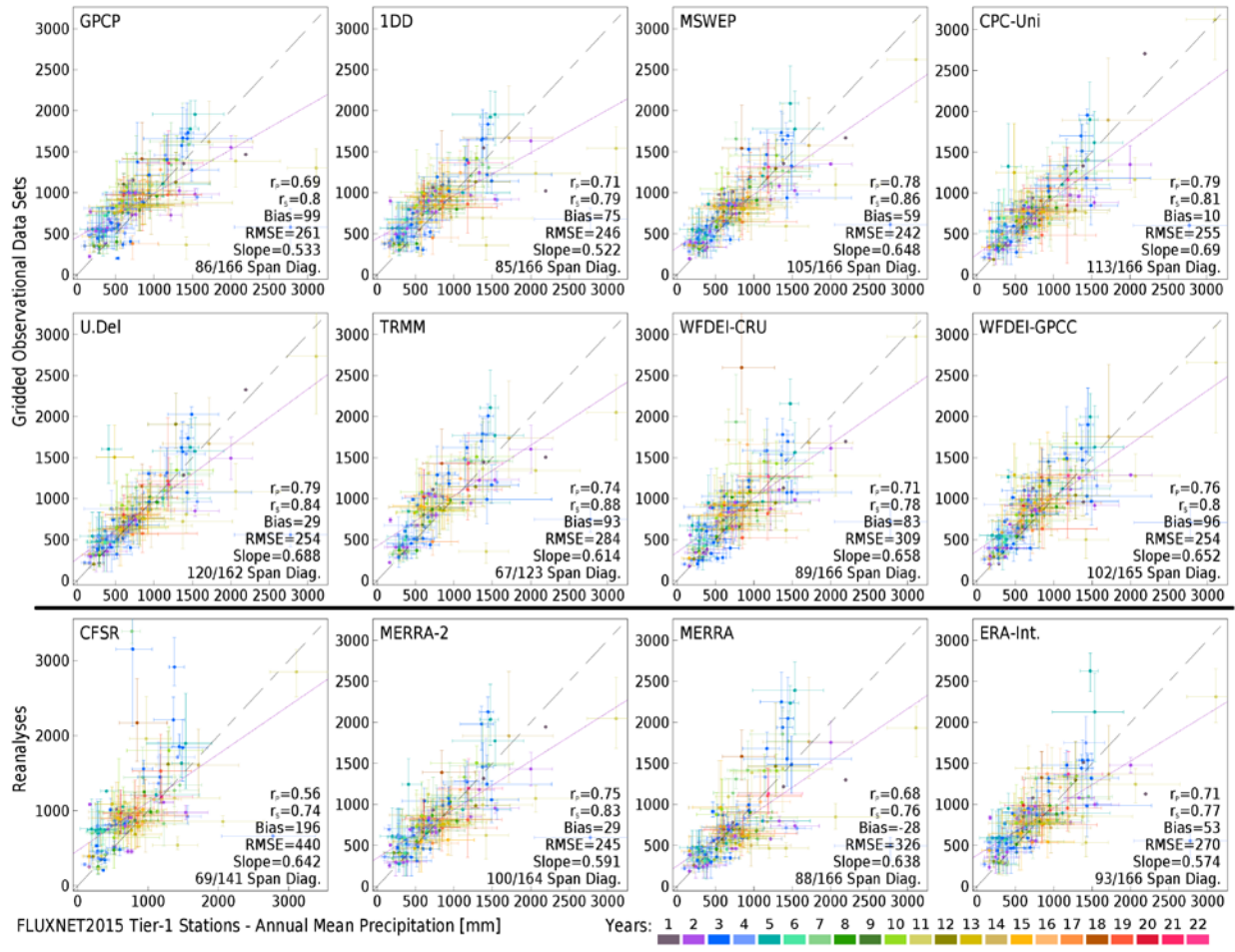
841



842

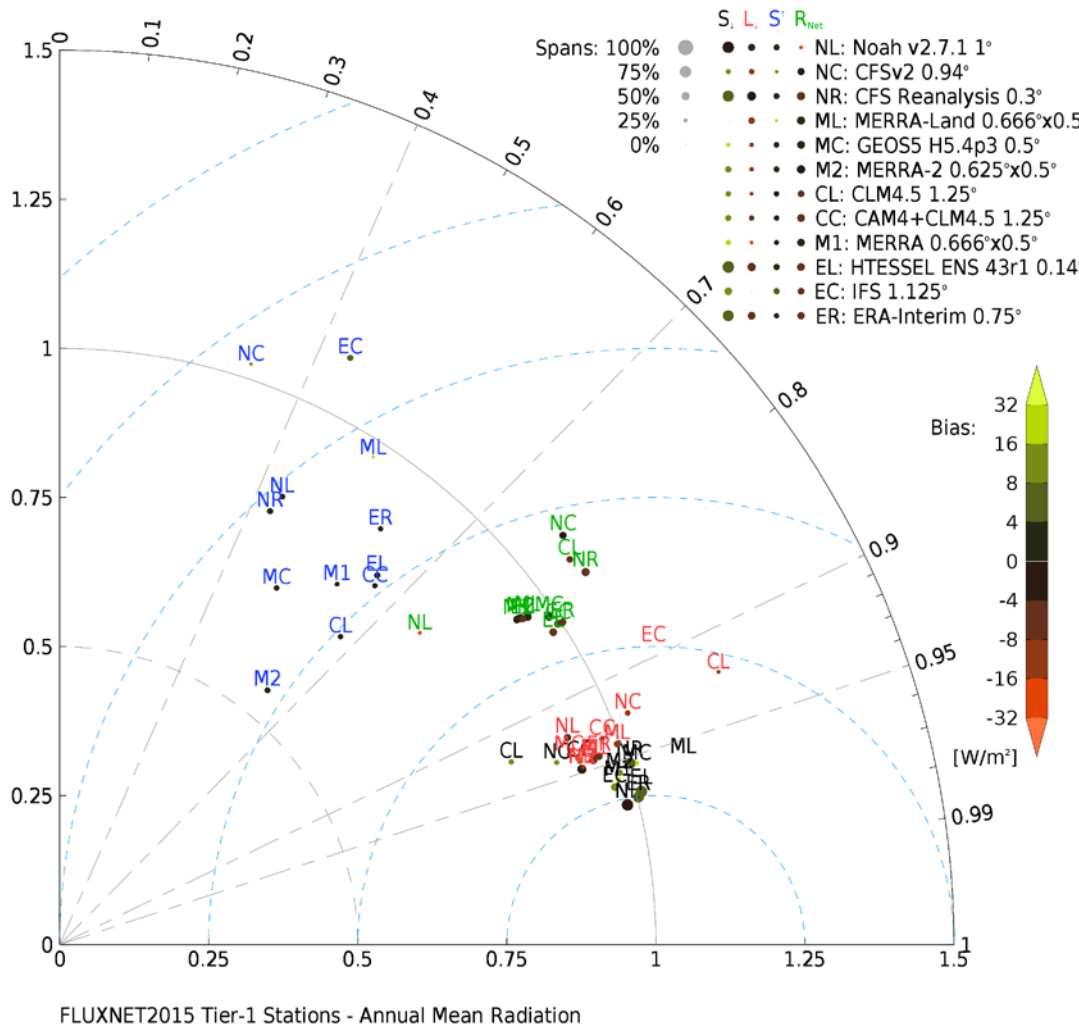
843 Figure 1: Location of the FLUXNET2015 Tier-1 sites used in this study. Triangles indicate  
 844 no upward shortwave radiation measurements available to estimate surface albedo, pluses  
 845 mean no Bowen ratio corrected surface heat fluxes provided, exes indicate neither albedo  
 846 nor corrected heat fluxes are available, circles have both. Color of the symbol indicates the  
 847 length of data series available.

848



849

850 Figure 2: Scatter of annual total precipitation measurements at FLUXNET2015 sites  
 851 to estimates (ordinate) from gridded observationally-based precipitation  
 852 analyses (top two rows) or reanalyses constrained by data assimilation (bottom row)  
 853 using the value from the grid box containing the FLUXNET2015 site location (unless data  
 854 are missing or indicated to be an all-ocean grid box). Dash-dotted diagonal grey line  
 855 indicates  $X=Y$ . Colors indicate years of available data from each FLUXNET2015 site,  
 856 whiskers span range of annual totals from FLUXNET2015 (horizontal) or gridded  
 857 estimates (vertical) for years where data sets overlap. Purple line is the best-fit linear  
 858 regression of Y on X. Statistics are explained in the text.  
 859

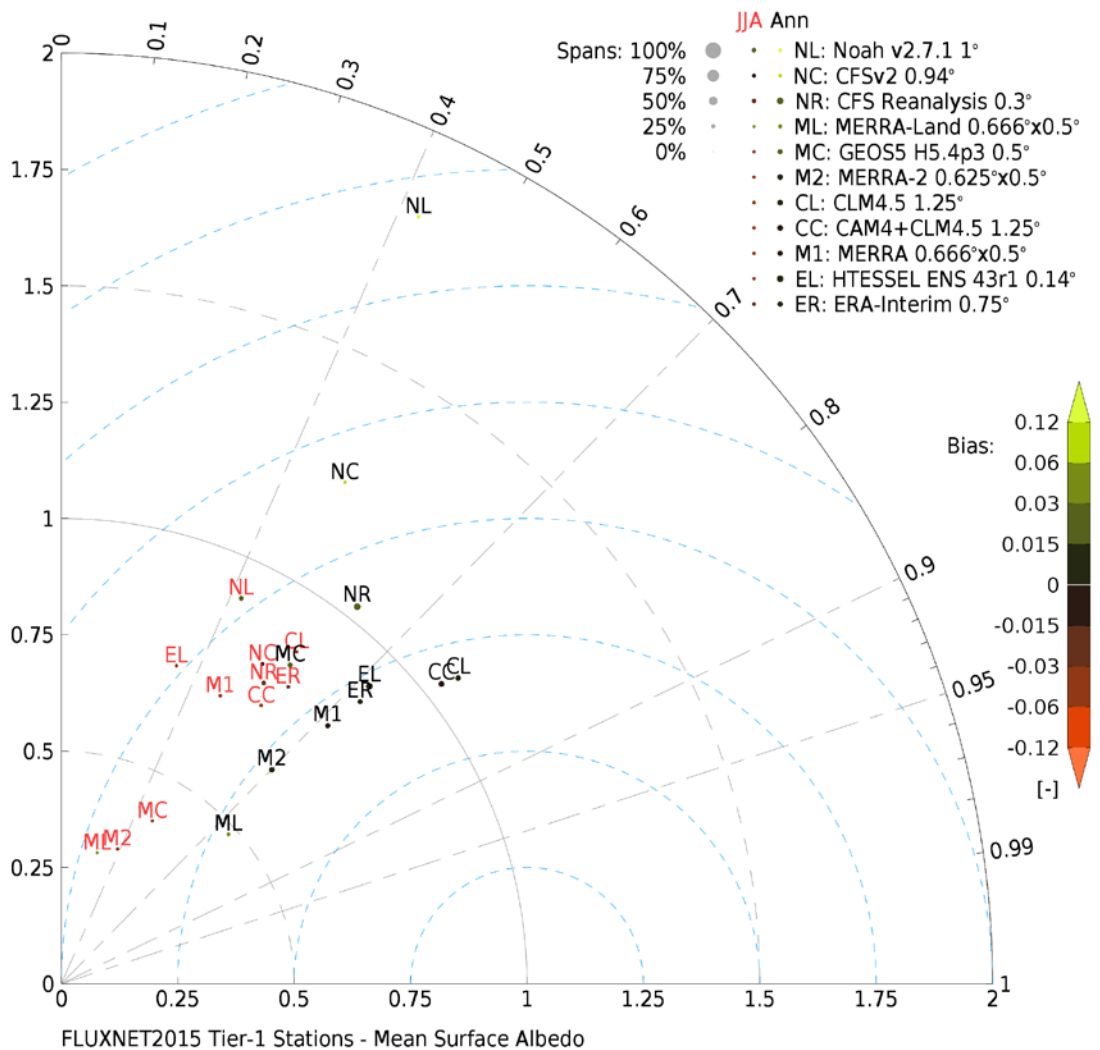


860

861 Figure 3: Taylor diagram of annual mean surface radiation terms for the 12 indicated  
 862 models verified against FLUXNET2015 sites for downward solar radiation (black),  
 863 downward longwave radiation (red), upward shortwave radiation (blue) and net radiation  
 864 (green). Dot colors indicate mean bias and size shows percentage of stations where the  
 865 range of the annual totals from the model overlaps the span from FLUXNET2015 sites (also  
 866 presented in tabular form in the upper right).

867

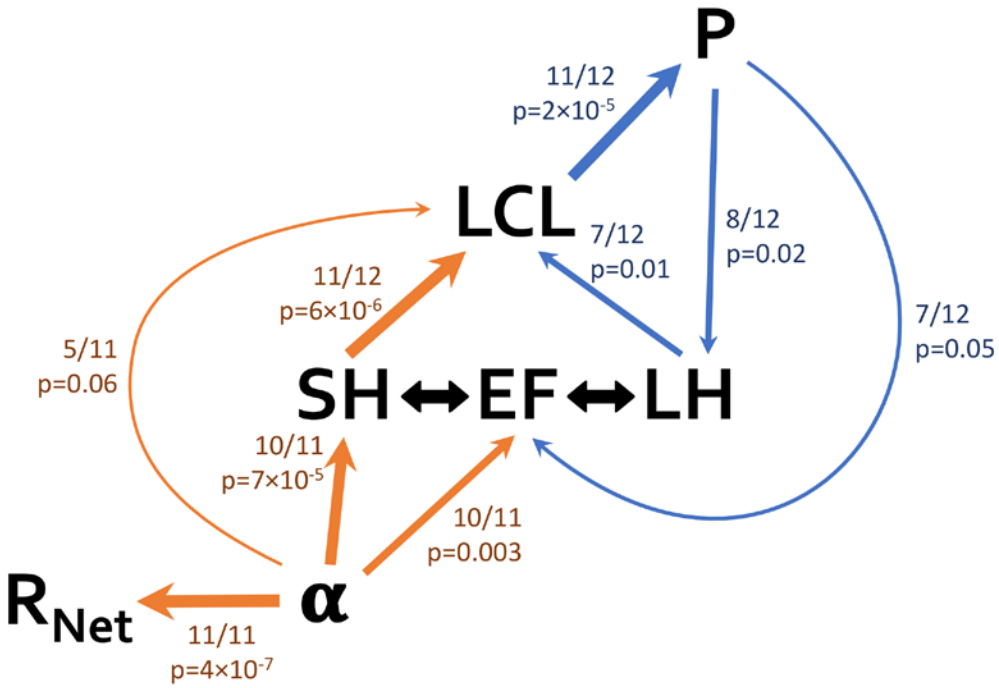
868



869

870 Figure 4: As in Fig. 3 for surface albedo; annual mean (black) and boreal summer (JJA)  
 871 mean (red).

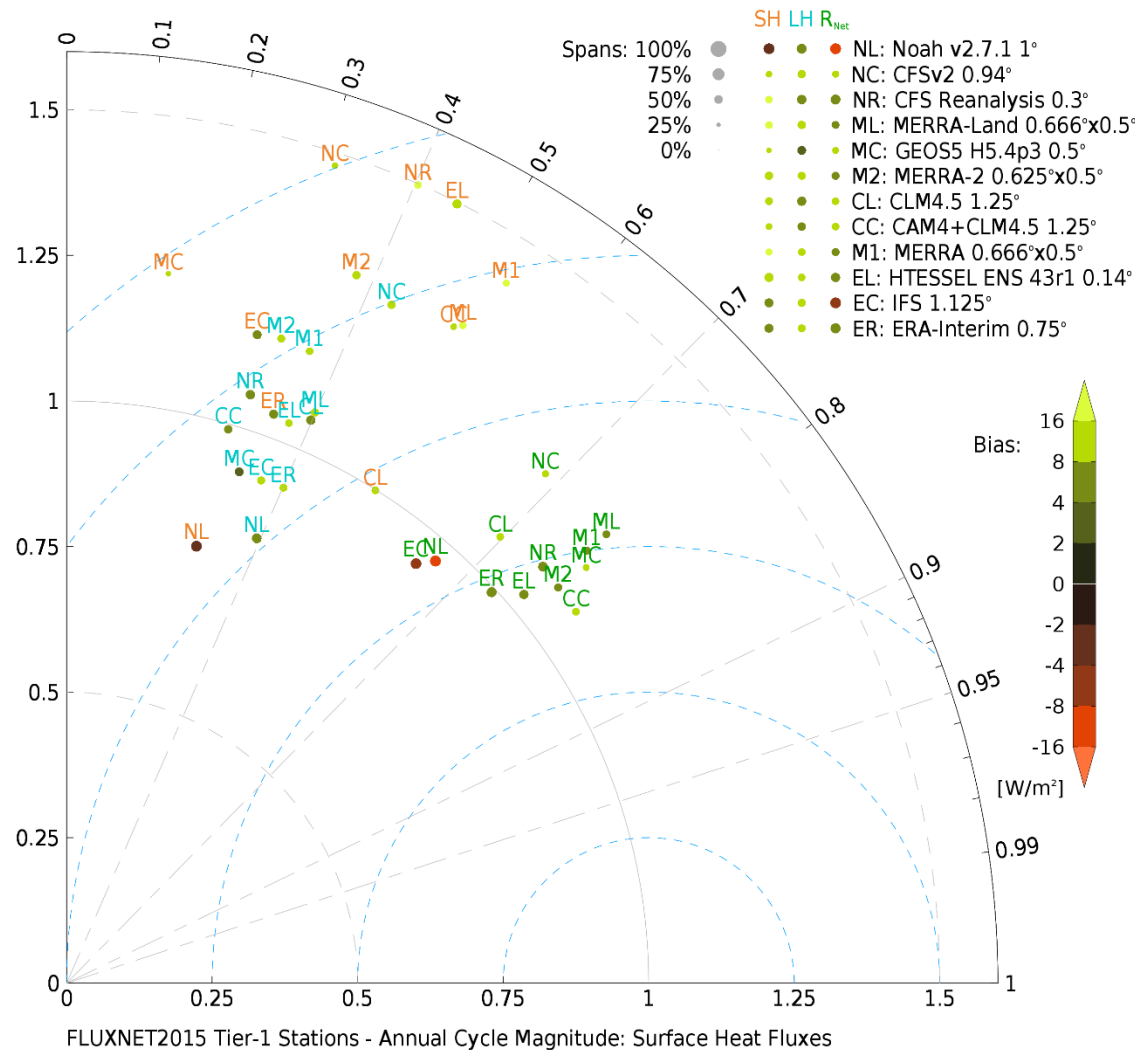
872



873

874 Figure 5: Propagation of errors estimated from their rank correlations among precipitation  
 875 (P), height of the lifting condensation level (LCL), evaporative fraction (EF), sensible and  
 876 latent heat flux (SH & LH), surface albedo ( $\alpha$ ) and net radiation ( $R_{Net}$ ) across  
 877 FLUXNET2015 stations. Ratios show the number of models out of 11 (correlations  
 878 involving  $\alpha$ ) or 12 (other variables) with p-values below 0.10; p-value shown is based on  
 879 the average of correlations across all models. Widths of arrows follow significance of  
 880 correlations and no arrows are drawn where p-values are large. The wide double arrows  
 881 between EF and heat fluxes denote p-values  $< 10^{-12}$ .

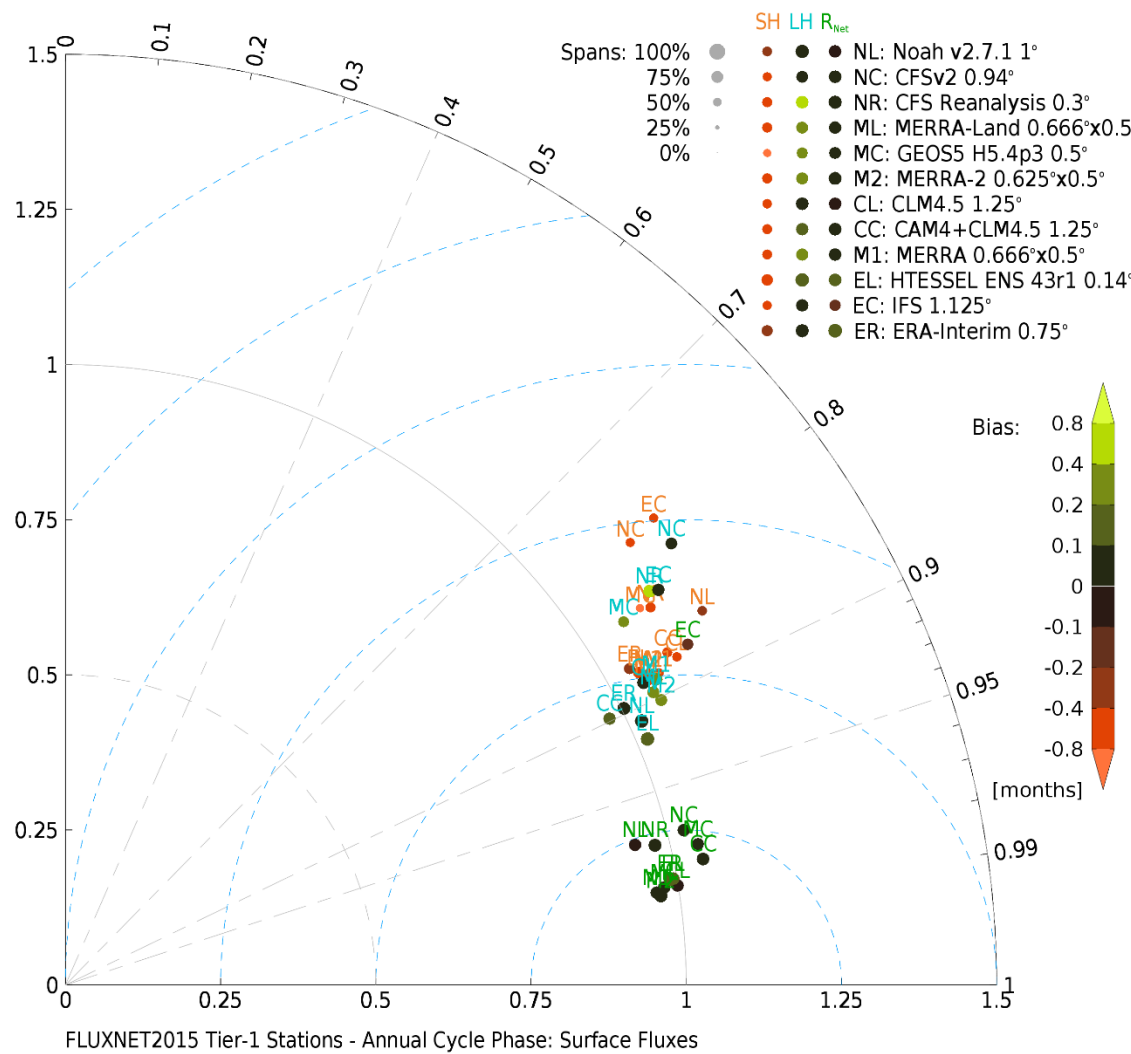
882



883

884 Figure 6: As in Fig. 3 for the magnitude of the annual cycle (first harmonic calculated from  
 885 monthly means) of sensible heat flux (orange), latent heat flux (cyan) and net radiation at  
 886 the surface (green).

887

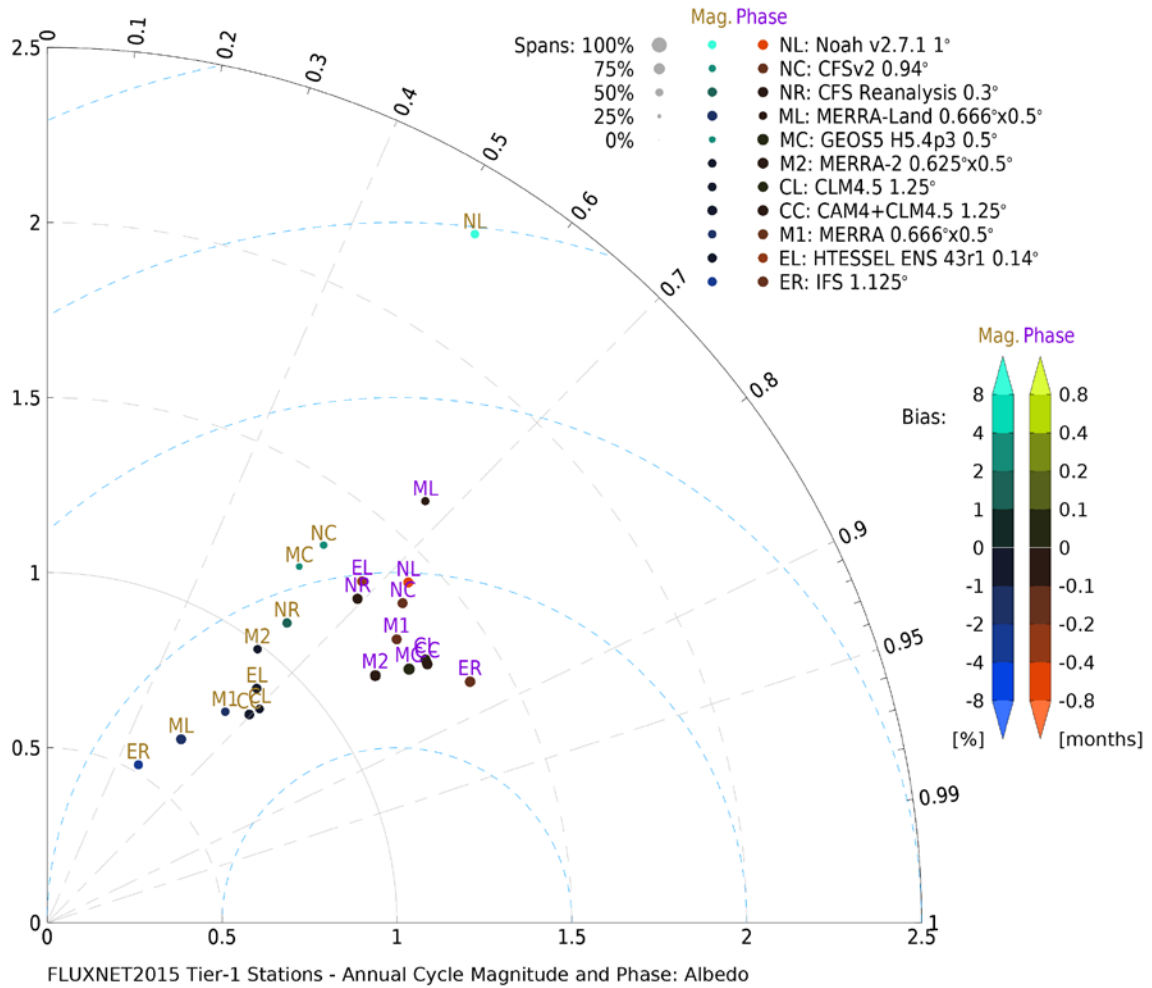


888

889 Figure 7: As in Fig. 6 for phase of the annual cycle of sensible heat flux (orange)

890 latent heat flux (cyan), and net radiation at the surface (green).

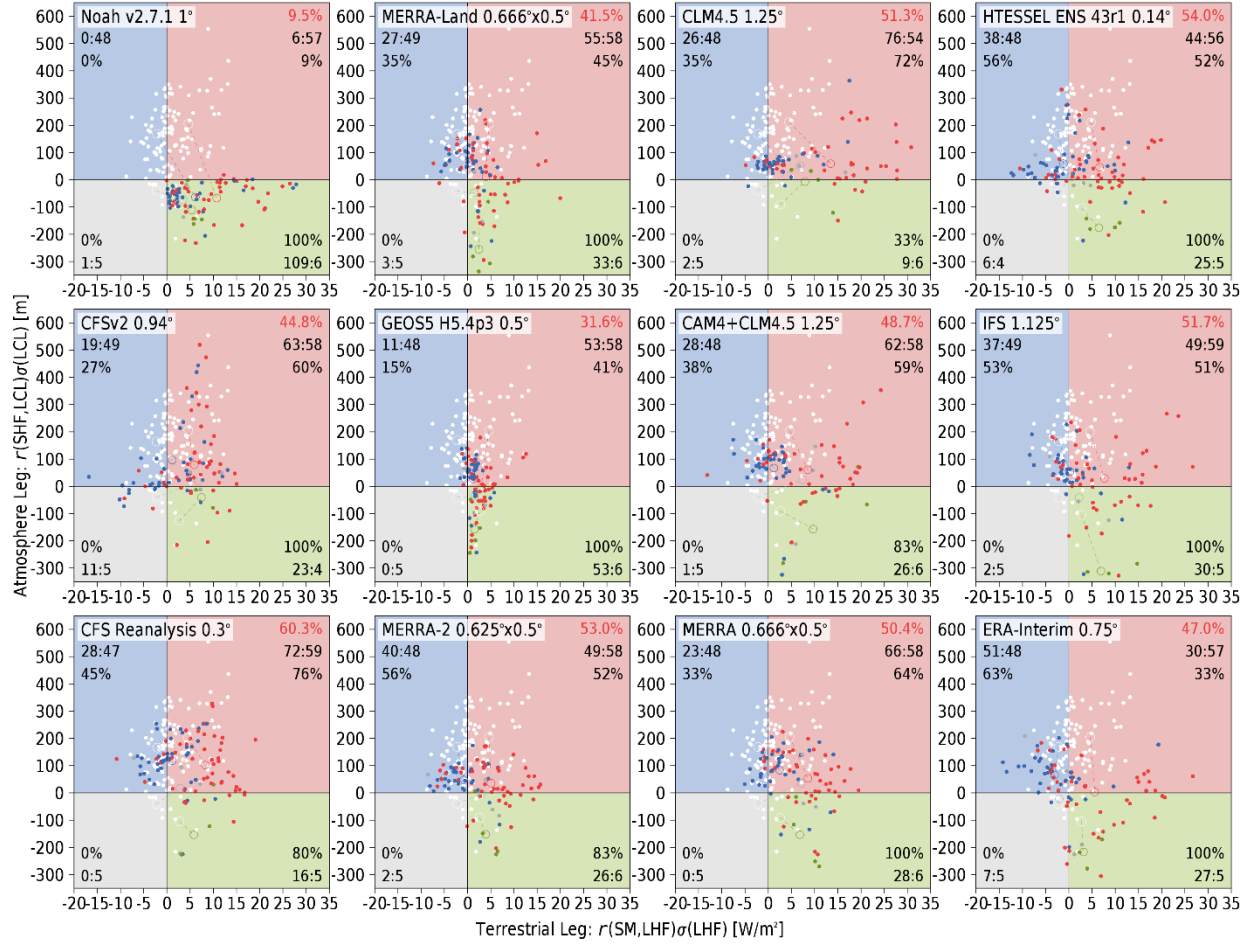
891



892

893 Figure 8: As in Fig. 6 for the magnitude (brown) and phase (purple) of the annual cycle of  
 894 surface albedo.

895



896 Figure 9: Distribution of coupling indices for the terrestrial (x-axis) and atmospheric (y-axis)  
 897 axis) legs for the warmest consecutive 3 months of the annual cycle for FLUXNET2015 sites  
 898 (white dots; identical in each panel) and for each model as indicated. Colors of dots indicate  
 899 in which quadrant that FLUXNET2015 site lies: red = both indices positive; green =  
 900 terrestrial positive, atmospheric negative; blue = atmospheric positive, terrestrial  
 901 negative; grey = both negative. The white circle indicates the centroid of all FLUXNET2015  
 902 stations that are in that quadrant, connected by a colored dotted line to a colored circle that  
 903 is the centroid of the same stations' corresponding grid boxes as simulated by the model.  
 904 Numbers in the corners of each quadrant show the number of points in that quadrant  
 905 according to the model and FLUXNET2015 data, separated by a colon, and the percentage  
 906 of the FLUXNET2015 sites within that quadrant that the model placed in the same  
 907 quadrant. The percentage in red at the upper right of each panel is the overall percentage of  
 908 sites where model and FLUXNET2015 agree on the quadrant.